

Oblique contraction along the fastest ocean-continent transform plate boundary focuses rock uplift west of the Fairweather fault, southeast Alaska

rwitter sr¹

¹Affiliation not available

April 16, 2024

Running Head: Rock uplift west of the Fairweather fault, Alaska

R.C. Witter¹, H.M. Kelsey², R.O. Lease¹, A.M. Bender¹, K.M. Scharer³, and P.J. Haeussler¹, and D.S. Brothers⁴

¹U.S. Geological Survey Alaska Science Center, Anchorage, AK, USA

²Department of Geology, Cal Poly Humboldt, Arcata, CA, USA

³U.S. Geological Survey Earthquake Science Center, Pasadena, CA, USA

⁴U.S. Geological Survey, Pacific Coastal and Marine Science Center, Santa Cruz, CA, USA

Abstract [286/300 words]

Contraction along the Yakutat-(Pacific)-North America plate boundary drives extreme rock uplift along Earth's fastest slipping (49 mm/yr) ocean-continent transform fault, the Fairweather fault. Between Icy Point and Lituya Bay, the near-vertical Fairweather fault focuses rock uplift and rapid right-lateral slip by accommodating both vertical and fault-parallel strain during ruptures with a substantial vertical-slip component and separate, predominantly strike-slip events. We use 1.0 m resolution digital elevation models and offshore seismic reflection profiles to map active faults, uplifted marine and fluvial terraces, and document past reverse fault earthquakes with maximum 3–5 m of coseismic uplift per event. Radiocarbon and luminescence dating provide timing to estimate 4.6–9.0 mm/yr Holocene rock uplift rates, which match 5–10 km/Myr Quaternary exhumation rates estimated from thermochronometry. These unusually high uplift rates result from plate-boundary strain that is partitioned onto reverse faults that form, together with the steeply dipping Fairweather fault, a 10-km-wide, asymmetric, positive flower structure along a 20°, ~30-km-long restraining double bend in the Fairweather fault. The principal reverse fault in the flower structure is the offshore, blind Icy Point-Lituya Bay fault, which ruptures no more than every 460–1040 years evidenced by uplifted Holocene marine shorelines. Evaluated over a range of dips, the uplift on this reverse fault implies maximum 3.1–10 m dip slip per event and estimated earthquake magnitudes of M_w 7.0–7.5. Our model implies oblique slip on the Fairweather fault at seismogenic depths with and without co-rupture on the reverse fault. Oblique slip on the Fairweather fault is evident where it vertically offsets fluvial and marine terraces by >25 m, strikes >20° west of plate boundary motion, juxtaposes near-surface rocks of different strength, and where the Yakutat block collides obliquely into North America.

1 Introduction

The Queen Charlotte–Fairweather Fault System—the fastest slipping ocean-continent strike-slip fault on Earth (Molnar and Dayem, 2010; Brothers et al., 2020)—defines the western North America plate boundary

in southeastern Alaska and western Canada. The Fairweather fault traces the northern 250 km of this fault system and accommodates >90% of the 53 mm/yr motion between the North America plate and the Yakutat block (Plafker et al., 1978; Brothers et al., 2020; Elliott and Freymueller, 2020). The Yakutat block, an overthickened oceanic plateau (Plafker, 1987; Lahr and Plafker, 1980; Bruns, 1983), is tectonically coupled to the Pacific Plate along the Transition fault (Eberhart-Phillips et al., 2006; Christeson et al., 2010) and both plates collide into southern Alaska (Figure 1). Transpression along the northeastern margin of the Yakutat block, where Cretaceous-Cenozoic sedimentary rocks obliquely collide with Chugach metamorphic rocks of the Fairweather Range, focuses extreme rates of horizontal and vertical deformation west of the Fairweather fault.

The 1958 moment magnitude (M_w) 7.8 Fairweather earthquake nucleated at 16 ± 4 km depth just north of Cross Sound (Doser and Lomas, 2000; Doser, 2010) near the southern end of the Fairweather fault where the plate boundary bends $\sim 20^\circ$ offshore to the Queen Charlotte fault (Figures 1 and 2). The fault ruptured toward the northwest through a restraining double bend (terminology after Crowell (1974)) between Icy Point and Crillon Lake (Witter et al., 2021), and continued breaking >260 km of the Fairweather fault to at least the latitude of Yakutat Bay (Doser, 2010). The 1958 focal mechanism indicates a steep ($88^\circ E$) fault plane striking 340° northwest, similar to the 337° strike of the linear Queen Charlotte fault trace in the seafloor (Brothers et al., 2020). Fault rupture stepped on land at Icy Point and induced 3.5–6.5 m right-lateral surface displacements on near-vertical faults striking 318° – 322° (Tocher, 1960) through

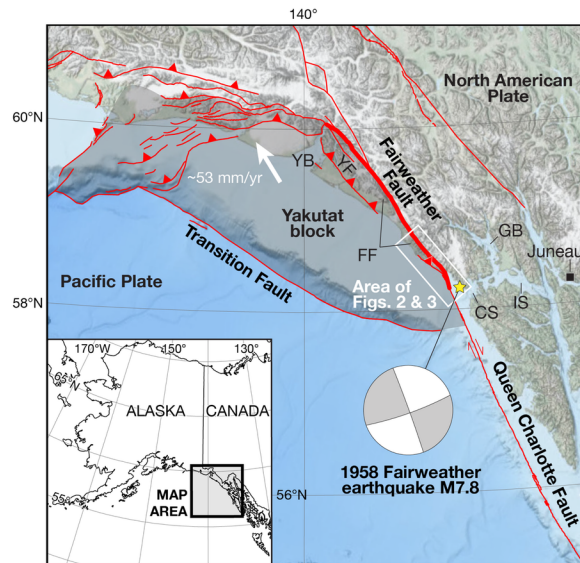


Figure 1. Active faults (red lines, barbs point down dip) along the Pacific-Yakutat-North American plate boundary where the Queen Charlotte fault steps onshore and becomes the Fairweather fault (bold red line). The 1958 M_w 7.8 Fairweather fault rupture extended >260 km (bold red line); the earthquake epicenter (star) is located near Cross Sound (Doser and Lomas, 2000; Doser, 2010). Yakutat block geodetic velocity from Elliott and Freymueller (2020). CS, Cross Sound; FF, Fairweather Foothills; GB, Glacier Bay; IS, Icy Strait; YB, Yakutat Bay; YF, Yakutat Foothills. Source of basemap: General Bathymetric Chart of the Oceans, <https://www.gebco.net/>; NOAA National Centers for Environmental Information, <https://www.ncei.noaa.gov/maps/bathymetry/>.

the restraining double bend. However, Icy Point, a peninsula beveled by late Pleistocene and Holocene marine and fluvial terraces at the southern end of this complex restraining double bend, conspicuously lacked evidence for vertical displacement during the 1958 earthquake (Tocher, 1960).

The tectonic geomorphology at Icy Point (Witter et al., 2021), an area of unusually high (5–10 mm/yr)

Quaternary rock uplift rates (Mann, 1986; Lease et al., 2021), presents a unique setting to investigate high-rate deformation along a major transpressional plate boundary fault system. The principal strand of the southern Fairweather fault accommodates >90% of plate boundary strike-slip motion (Elliott and Freymueller, 2020) and structurally controls vertical uplift along the eastern flank of the Icy Point peninsula (Witter et al., 2021). Previous studies implicate a west-vergent reverse fault offshore and west of Icy Point as the mechanism driving marine terrace uplift (Plafker, 1967, 1971; Carlson et al., 1988). However, geomorphic evidence for vertical slip on the Fairweather fault raises several motivating questions, including: What fault rupture scenarios sustain such high uplift rates at Icy Point along one of the fastest strike-slip faults on Earth? What kinematic model of the Fairweather fault can account for both Holocene vertical displacement and the documented right-lateral surface fault rupture in 1958 that lacked coseismic uplift of Icy Point?

Here, we present the results of investigations at Icy Point to assess strain partitioning and the Holocene earthquake history along the southern Fairweather fault through the restraining double bend south of Lituya Bay (Figure 2). Using offshore and onshore observations, we assess how slip is partitioned on strike-slip and reverse faults in the complex corner of a restraining bend between the Queen Charlotte and Fairweather faults. We quantify rates of oblique contraction in the restraining bend that provide insights about how fault slip may vary on a principal, strike-slip fault and we propose a range of fault rupture scenarios occurring over multiple earthquake cycles that explain our observations. Our findings contribute a conceptual understanding of oblique contraction along the Fairweather fault that can both improve kinematic fault models and provide better tectonic context for paleoseismic data in southeastern Alaska that underpin seismic hazard assessments.

2 Seismotectonic and geologic setting

2.1 A transpressional plate boundary in southeast Alaska

The Fairweather fault juxtaposes the Yakutat block and the North America plate along >250 km of the curvilinear plate boundary that extends from Icy Point north-northwest to the vicinity of Yakutat Bay (latitude range 58.4°–60.0°N) (Plafker et al., 1978) (Figure 1). Witter et al. (2021) determined a Holocene slip rate of [?]49 mm/yr for the Fairweather fault at Crillon Lake (29 km north-northwest of Icy Point) from analyses of multiple offset fluvial channels cut into till and outwash, which is similar to the ~53 m/kyr slip rate estimate for the offshore Queen Charlotte fault 50 km to the southeast (Brothers et al., 2020). Elliott and Freymueller (2020) used horizontal crustal velocities from satellite geodesy to devise a block model that implies 44–46 mm/yr of right-lateral strike-slip motion between the Yakutat block and North America accommodated on the Fairweather fault. This decadal slip rate amounts to >90% of the strike-slip motion along the eastern margin of the Yakutat block. Block model results of Elliott and Freymueller (2020) also imply convergence normal to the plate boundary on reverse faults that build topography immediately west of the Fairweather fault.

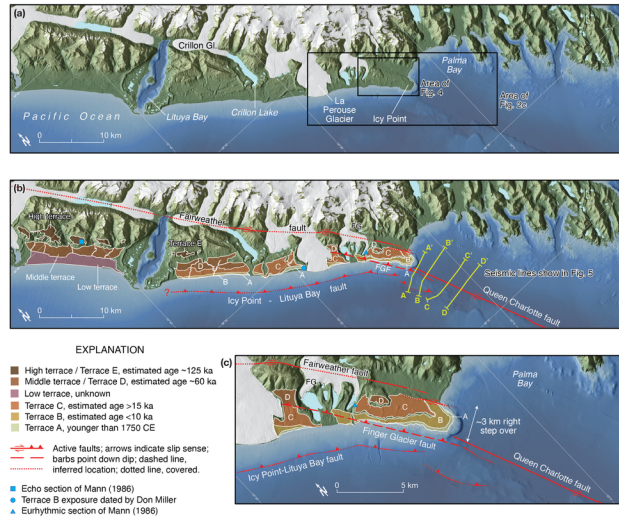


Figure 2. (a) Topographic and bathymetric digital elevation models along the Gulf of Alaska coast in the area surrounding Lituya Bay and Icy Point. The bathymetric compilation includes NOAA data (<https://www.ncei.noaa.gov/maps/bathymetry/>) in the Gulf of Alaska (100-m resolution) and Lituya Bay (15-m resolution). Ten-meter resolution data in Palma Bay, the area offshore Icy Point and along the Queen Charlotte fault comes from recent multibeam surveys in 2015 (Dartnell et al., 2022). Topographic data come from the 5-m resolution Alaska IFSAR digital elevation model (<https://elevation.alaska.gov/>). (b) South of Palma Bay, bathymetric data show the linear, submarine trace of the Queen Charlotte fault, which projects northwest toward Icy Point. The linear Queen Charlotte fault trace terminates near a series of folds expressed on the sea floor 5-10 km south of Icy Point. Onshore, the Fairweather fault borders the eastern edge of the uplifted Icy Point peninsula and strikes ~20° more westerly than the Queen Charlotte fault offshore. West of the Fairweather fault, the Finger Glacier fault (FGF) and the inferred Icy Point-Lituya Bay fault (Plafker, 1971; Carlson et al., 1988) are the northwestern extensions of faults imaged in seismic reflection profiles. Coastal geomorphology preserves remnants of six marine terraces identified by Mann (1986). Cyan symbols locate key exposures of marine terraces described by Mann (1986) and dated by Don Miller (Rubin and Alexander, 1958).

High topography along the coast north of Icy Point, named informally here as the ‘Fairweather Foothills,’ reflects contraction west of the Fairweather fault (Figure 1). The Fairweather Foothills continue northward for 200 km, locally exceeding elevations of 1300 m, and merge with the Yakutat Foothills, which are bound by an active reverse fault along their southwest flank (Bruhn et al., 2004). Convergence occurs at the northern end of the Fairweather fault on mapped reverse faults in the Yakutat Foothills (Bruhn et al., 2004). The primary reverse fault is variously called the Yakutat fault (Schartman et al., 2019; Walton et al., 2022), the Yakutat Bay thrust fault (Bruhn et al., 2004; Plafker and Thatcher, 2008), and the Foothills fault (Elliott et al., 2010); in all cases, the fault delineates the western margin of the Yakutat Foothills (Figure 1). Bruhn et al. (2004) described the Yakutat fault as part of a system of faults that form an asymmetric flower structure (terminology after Sylvester and Smith (1976)), which accommodates contractional deformation southwest of the structural syntaxis at the northern end of the Fairweather fault (Bruhn et al., 2012). In a block model by Elliott and Freymueller (2020), the fault accommodates 5.4 ± 0.7 mm/yr of contraction and connects to the offshore Icy Point-Lituya Bay fault, which is discussed in the next section.

Lease et al. (2021) provide geologic context for the convergence modeled by Elliott et al (2010) and Elliott and Freymueller (2020) by estimating exhumation rates along the restraining bend and further north along the plate margin. Lease et al. (2021) conclude that the flight of emergent marine terraces at Icy Point imply >6–8 km/Myr rock uplift rates along the Fairweather fault restraining double bend. Northwest of the restraining bend, rock uplift in the Fairweather Foothills reflects transient, rapid exhumation of rock

advected through the Fairweather fault restraining bend where the Icy Point-Lituya Bay fault branches from the Fairweather-Queen Charlotte fault. The rocks that underlie high topography of the Yakutat and Fairweather foothills suggest a long-term strike-slip rate of ~ 54 km/Myr since ~ 3 Ma (Lease et al., 2021).

2.2 Geology of the Icy Point peninsula and the offshore Icy Point-Lituya Bay thrust fault

At Icy Point, the Fairweather fault juxtaposes rocks of considerably different ages, rock types, and strengths (Figure 3). East of the fault, Paleogene amphibolite-facies and layered gabbro metamorphic rocks, >9 -km-thick, support the high topography of the Fairweather Range; west of the fault, Cretaceous-Cenozoic sedimentary rocks, ~ 12 km thick, overlie the eastern Yakutat block (Plafker, 1994). The Tertiary rocks at Icy Point include the Topsy Formation and the disconformably overlying Yakataga Formation. The Topsy Formation consists of marine concretionary siltstone and greenish-gray argillaceous and carbonaceous sandstone deposited during the Miocene (Miller, 1961; Plafker, 1967; 1971; 1987). The Yakataga Formation is as young as Pleistocene (Marincovich, 1980; Rau et al, 1983), and includes interbedded siltstone and sandstone that grade into overlying beds containing minor conglomerate and mudstone that incorporates ice-transported clasts of diverse lithologies (Plafker, 1967; 1971).

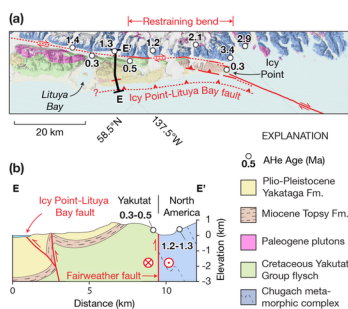


Figure 3. (a) Geology along the Fairweather fault in Glacier Bay National Park (Wilson et al., 2015). A restraining bend between Lituya Bay and Icy Point coincides with the onshore transition from strike slip to oblique slip, which drives uplift west of the fault. (b) Cross section depicting 4–6 km of structural relief across the eastern Yakutat microplate (Plafker, 1971) and geologic contrast with North America (Loney and Himmelberg, 1983). Thermochron AHe data from Lease et al., (2021). Fm.—formation.

Plafker (1971) inferred a major thrust or reverse fault offshore of Icy Point on the basis of well-exposed, steeply overturned bedding in the Topsy and Yakataga Formations:

”The narrow belt of Tertiary rocks south of Lituya Bay is folded into a shallow syncline and a highly asymmetric faulted anticline [and] these folds pass to the southeast into a seaward-facing homocline which is nearly vertical or slightly overturned. The south limb of the anticline is believed to be cut by an unexposed thrust or reverse fault that strikes parallel to the coast.”

Plafker (1967; 1971; 1987) mapped the fault offshore and very near the coast to explain steeply dipping sedimentary rock as young as Pleistocene (Figure 3). This interpretation seems reasonable because such moderate-to-steep uniform dips occur in layered rocks on the hanging walls of reverse faults in other contractional settings, including oblique-slip tectonic environments (Avé Lallemand et al., 1987; Bartley et al., 1990; Namson and Davis, 1990; Suppe and Medwedeff, 1990). Although unable to verify the presence of an offshore fault, Plafker (1967) depicted the ”unexposed thrust or reverse fault” in his 1967 geologic map. He also drew a cross section (Plafker 1971; 1987) showing as much as 4-6 km of structural relief along the northwestern edge of the Yakutat block where it abuts the Fairweather fault (Figure 3).

The contractional deformation that Plafker (1971) inferred to exist offshore to the west of Icy Point is evident in seismic reflection data. Early marine seismic data collected along two northeast-trending track lines offshore 6 km south of Icy Point (Bruns, 1983; Carlson et al., 1985; 1988) show deformed strata in

Miocene and younger sediment along strike to the south-southeast of Plaker’s inferred fault. Carlson et al. (1988) identified this inferred fault as the Icy Point-Lituya Bay fault. Further support for the existence of this structure are shallow seismic reflection profiles collected in 2015 and 2017 that show an east-side-up reverse fault offshore to the south-southwest of Icy Point (Balster-Gee et al., 2022a, b) (Figure 2). These seismic data constrain the near shore position of the Icy Point-Lituya Bay fault to within 3.5 km of the coast between Lituya Bay and Crillon Lake (Figure 2).

2.3 Marine Terraces Between Icy Point and Lituya Bay

Where a transpressional fault system occurs in a coastal setting, the ages of uplifted marine terraces can help to constrain rock-uplift rates at millennial time scales (Lajoie, 1986; Kelsey, 2015). Five marine terrace levels preserved along the 42 km of coast between Lituya Bay and Icy Point imply rapid uplift rates over the past 125,000 years (Figure 2) (Hudson et al., 2022; Ugolini and Mann, 1979; Mann and Ugolini, 1985; Mann, 1986). The terrace chronology is poorly resolved, and moraines of Pleistocene age indicate that glaciers advanced over the three oldest marine terraces southeast of Lituya Bay (Terraces C, D, and E) (Mann and Ugolini, 1985; Mann, 1986). The two youngest terraces (Terraces A and B) are largely free of glacial deposits other than moraines of Neoglacial age deposited along the margins of the North Finger and La Perouse Glaciers, and adjacent to Lituya Bay, which was most recently deglaciated shortly before 1700 CE (Mann and Ugolini, 1985). This section reviews the marine terrace geology and places our study into the context of prior work. Interpreting a dynamic glacial landscape on a rapidly uplifting coast requires the compilation of published maps of marine terraces between Lituya Bay and Icy Point, which we overlay onto the 5-m Alaska Digital Elevation Model topography (U.S. Geological Survey, 2016) to correlate terrace surfaces along shore using the naming scheme of Mann (1986) (Figure 2).

Terrace E, originally mapped by Mann (1986), is the oldest marine terrace between Lituya Bay and Icy Point. Deeply incised remnants of Terrace E, with a maximum shore-perpendicular width of ~1 km, extend ~5 km southeast of Lituya Bay (Figure 2). Based on its similar topographic position, Terrace E may have been coeval with the High Terrace present northwest of Lituya Bay (Figure 2b). A stratigraphic section in the High Terrace (Figure 2, Echo section of Mann (1986)) exposes a shore platform at an elevation of ~500 m overlain by several meters of beach sediment, above which are ~10 m of alluvial deposits, which in turn are overlain by 40 m of glacial outwash and then till (Mann, 1986). Wood in peat beds near the top of the alluvial unit yielded an enriched radiocarbon date of >72 ka (Mann, 1986; sample QL-1613). This non-finite ¹⁴C date and the fossil pollen flora within the peat led Mann (1986) to suggest that the High Terrace (and hence Terrace E southeast of Lituya Bay) records a RSL high stand during Marine Isotope Stage (MIS) 5e, the Last Interglacial, ca. 115 to 130 ka. Mann (1986) used these age constraints and the 500 m elevation of the High Terrace to estimate tectonic rates of uplift between 4–8 mm/yr.

Terrace D ranges in elevation from 60 to 100 m along the 20 km of coastline southeast of Lituya Bay (Figure 2b). At Icy Point it has a mean elevation of ~125 m and its width ranges from 0.6 to 2.5 km. The ~370-m vertical separation between marine Terrace D and older Terrace E indicates a substantial time passed between the formation of the two shore platforms. Although no chronologic data constrain the age of Terrace D, its much lower elevation, smoother geomorphic expression, and greater coastal extent compared to Terrace E suggest that it was cut during MIS 3 (65–30 ka), which saw several RSL high stands between 65 and 40 ka (Siddall et al., 2008). Along the Pacific coast of California, several MIS 3 marine terraces date to 40–60 ka (Simms et al., 2015). Mann (1986) estimated the age of Terrace D to be about 60 ka based on the uplift rate inferred for the High Terrace.

Terrace C ranges in elevation from 15 to 40 m within 20 km Lituya Bay and 65 to 100 m at Icy Point. It varies in width from 1.4 to 2.1 km. The minimum-limiting date on this terrace comes from the ¹⁴C age of wood obtained from an exposure in the glacial trough cut by the southernmost lobe of the Finger Glacier (Figure 2) (Mann, 1986). Here the shore platform of Terrace C crosscuts bedrock structures and is overlain first by several meters of marine sand and gravel. Above the beach deposits are some 50 m of till and outwash interbedded with multiple buried soils. A log found in the lowermost till unit ~10 m above the bedrock surface of the terrace indicates that ice advanced seaward onto Terrace C between 14,150–15,010 cal yr BP

(sample Beta-10647; $12430 \pm 100^{14}\text{C yr BP}$) (Mann, 1986). The superposition of the lower till over beach sand deposited on a shore platform implies that Terrace C formed prior to about 15 ka.

Moraines deposited on the surface of Terrace C during ancient fluctuations of the Finger Glacier system provide constraints on the maximum height reached by RSL during the Late Glacial (10–15 ka). Mann (1986) attributed the presence of arcuate “trains of massive, cavernously weathered, erratic boulders” on the surface of Terrace C to a marine transgression occurring sometime after the terrace was formed and either during or shortly after it was overridden by an extensive glacial advance. Today, at Icy Point, these erratic boulder trains on Terrace C are elevated as much as 80 m above modern sea level. Mann (1986) attributed the wave-washed modification of the moraines to erosion and scour by ocean waves when glacial isostatic depression raised RSL at some time after the Last Glacial Maximum. Stratigraphic evidence for ice advance over Terrace C at the Eurhythmic section described by Mann (1986) (Figure 2) and wave modification of recessional moraines suggest that RSL attained a height sufficient to modify moraines on Terrace C sometime after 14–15 ka.

Hudson et al. (2022) and Ugolini and Mann (1979) investigated the two youngest surfaces, Terraces A and B, southeast of Lituya Bay, but no past studies have described in detail the youngest two terraces at Icy Point. Terrace B, a time-transgressive surface (see section 4.2) that varies from 0.3 to 1.1 km wide, extends along 42 km of the coast between Lituya Bay and Icy Point at elevations ranging between 12 and 80 m. Hudson et al. (2022) estimated that Terrace B is 2–3 ka based on the ^{14}C ages of the deepest samples of peat accumulated on the terrace. However, Ugolini and Mann (1979) showed that the terrace peatlands form as a result of plant succession and soil development as terrace vegetation changes from beach meadows to forests to peat bogs on younger to older surfaces, respectively. Because accumulation of peat lags the time of terrace emergence, basal peat ages provide only minimum-limiting estimates on the timing of terrace emergence. The age of a “beach-worn” driftwood sampled by Don Miller (blue circle, Figure 2) at the base of a 3 m section of interbedded sand and gravel deposited on a shore platform at an elevation of 46 m indicates that Terrace B emerged before 2960–4060 cal yr BP (Rubin and Alexander, 1958, p. 127; sample W-405, $3250 \pm 200^{14}\text{C yr BP}$).

The lowest marine terrace southeast of Lituya Bay is Terrace A, a 150 to 675 m wide surface ranging in elevation up to 14 m that borders the present shoreline between Lituya Bay and Icy Point. At a site near the inland limit of Terrace A near Lituya Bay, Ugolini and Mann (1979) estimated the age of the surface at 400 years based on the numbers of annual rings in spruce trees. However, at Icy Point, Terrace A probably post-dates 1750 CE if, as proposed by Mann and Streveler (2008), abandoned beach ridges that define its backedge record a high-sea stand and subsequent glacial isostatic rebound after the Little Ice Age (LIA). During the LIA (1300–1900 CE), the expansion of glaciers in the Fairweather Range and Coast Mountains (McKenzie and Goldthwait, 1971) caused widespread isostatic depression across the region (Motyka, 2003; Larsen et al., 2005). LIA isostatic depression caused ~ 4 m of RSL rise on both sides of the Fairweather fault (Mann and Streveler, 2008), which between Lituya Bay and Icy Point submerged and eroded the lowest, formerly subaerial portions of Terrace B. Starting ~ 1750 CE, rapid downwasting of the regional glacier cover triggered rapid isostatic rebound and a fall in RSL that formed Terrace A, which continues today at rates approaching 30 mm/yr in Glacier Bay (Larsen et al., 2005) and 16–18 mm/yr near Icy Point (Elliott et al., 2010).

2.4 The 1958 Fairweather earthquake effects at Icy Point

Post-earthquake surveys of the ground rupture effects happened within days of the 1958 earthquake (Tocher and Miller, 1959; Tocher, 1960). Although most of the rupture occurred under ice or water, windows of ice-free terrain between Crillon Lake and Icy Point revealed evidence for surface deformation consisting of predominantly right-lateral displacement (Tocher and Miller, 1959). Right-lateral offset averaged ~ 3.5 m along the fault rupture between Crillon and La Perouse Glaciers (Figure 2), where surface displacement could be measured, but one site stood out: northeast of Crillon Lake Tocher (1960) measured 6.6 m of right-lateral and 1.1 m vertical offset where the fault cuts a late Holocene alluvial fan (Witter et al., 2021). However, Tocher noted that west-side-up coseismic motion in 1958 was atypical, “The dip-slip component was evident

only at this one locality” (p. 289, Tocher, 1960).

During fieldwork one year later at Icy Point, Tocher (1960) measured ~3 m of right-lateral offset across a shear zone, including 2.4 m of right-lateral offset on a fault striking N38°W and dipping 90° exposed in a “narrow gulch cut into bedrock.” Here again, evidence for substantial coseismic vertical displacement during the 1958 fault rupture is equivocal based on Tocher’s report: “No ground breakage was detected on the terrace surface adjacent to the gulch, even directly in line with the 8-foot (2.4 m) offset.” Because Tocher did not report any vertical offset, we assume that if surface fault rupture at Icy Point included a vertical component, then it was too little to detect.

Here, we aim to reconcile an apparent contradiction between the geomorphic record of late Pleistocene Icy Point uplift and the dominantly horizontal slip observed on the Fairweather fault in 1958. Although the Fairweather earthquake induced little-to-no permanent vertical displacement at Icy Point in 1958, repeated episodes of coseismic vertical displacement are required, as indicated by the emergence of marine terraces that bevel the peninsula and are bounded on the east by the 25-m tall, west-side-up Fairweather fault scarp.

3 Research approach

To assess the kinematics of rupture and slip partitioning on the Fairweather fault, we used multiple approaches including interpretation of recently-acquired lidar topography, digital and field-based geomorphic mapping, high-resolution multibeam bathymetry and multichannel seismic reflection surveys, and both radiocarbon accelerator mass spectrometry (AMS) and infrared stimulated luminescence (IRSL) techniques to estimate the ages of Holocene landforms.

Lidar data acquired in 2015 (Witter et al., 2017a) provided 1-m-per-pixel bare-earth digital elevation models that inform our interpretations of tectonic geomorphology and coastal and glacial landforms. Using a helicopter-mounted lidar system, the U. S. Geological Survey and collaborators (Acknowledgments) collected lidar data in three ice-free sections of the Fairweather fault within 33 km northwest of Icy Point (Witter et al., 2017b). Here, we focus on the southern lidar map, a 9 by 5 km area that includes the Icy Point peninsula and extends north-northwest to where the Fairweather fault crosses the southern-most Holocene moraines of the Finger Glacier. Elevations have ± 0.10 m accuracy and are reported as NAVD 88 orthometric heights.

Geomorphic maps (Figure 4) developed from lidar topography and 2014–2015 satellite imagery guided our field investigations in May-June 2017. Prior to the fieldwork, we mapped uplifted terraces and candidate fault scarps on lidar and satellite imagery. Fieldwork involved establishing ground-based geodetic surveys to field check lidar DEMs, collecting Miocene-to-Pleistocene rock samples for a fault-perpendicular thermochronometry transect (Lease et al., 2021), verifying fault traces of the Fairweather fault, coring or excavating exposures in uplifted beach deposits on Terraces A and B, describing degree of soil development on Terraces A and B, describing fluvial and tidal-slough deposits that inform RSL changes, and collecting samples for radiocarbon and luminescence age analyses.

Between 2015 and 2017 the USGS led a series of marine geophysical surveys offshore and to the south of Icy Point to map the seafloor morphology of the Queen Charlotte fault and image the stratigraphy and structure along the entire continental shelf and slope to the U.S.-Canada international border. Multibeam bathymetry data (gridded to 10-m resolution DEM) (Dartnell et al., 2022) and a dense grid of high-resolution multichannel seismic profiles (Balster-Gee et al., 2022a, b) were collected across the Queen Charlotte fault aboard the R/V Solstice in 2015 in the region between Icy Point and Cross Sound, and then again in 2017 aboard the R/V Ocean Starr (Brothers et al., 2020). The multichannel seismic profiles were processed using the commercial software *Shearwater Reveal*; faults, folds and seismic stratigraphy were imaged to sub-bottom depths of several hundred meters depending on the substrate geology and water depth.

We used a combination of infrared-stimulated luminescence (IRSL) and AMS radiocarbon age analyses to estimate the Holocene ages of coastal landforms and terrace deposits at Icy Point (Witter and Bender, 2021). The terrace deposits lacked wood or charcoal, so we employed IRSL analyses of feldspar grains to estimate ages of sandy beach and aeolian deposits. IRSL-derived ages indicate the last time that the deposit

was exposed to sunlight (Aitken, 1998). We sampled according to the procedures as outlined in Gray et al. (2015). IRSL analyses (Table 1) were performed by the Utah State University Luminescence Laboratory using the single-aliquot regenerative-dose procedure of Wallinga et al. (2000) on 2mm small-aliquots of feldspar sand at 50°C. The IRSL age on each aliquot is corrected for fading following the method of Auclair et al. (2003) and using the correction model of Huntley and Lamothe (2001). The equivalent dose (DE) and IRSL age are calculated using the Central Age Model (CAM) or Minimum Age Model (MAM) of Galbraith and Roberts (2012).

Radiocarbon (^{14}C) AMS analyses (Witter and Bender, 2021) were used to estimate the ages of fluvial and tidal-slough deposits. Dated material included individual rings of in-growth-position tree stumps, conifer needles and cones, detrital wood, and herbaceous material. We use OxCal (version 4.4.2, Bronk Ramsey, 2009; 2023) and the IntCal20 atmospheric ^{14}C curve (Reimer et al., 2020) to calibrate ^{14}C dates reported in this study as well the ^{14}C dates published by Rubin and Alexander (1958) and Mann (1986), which constrain ages of marine terraces. Calibration of a radiocarbon date of a marine bivalve shell from Terrace A beach deposits uses the Marine20 calibration curve (Heaton et al., 2020) and incorporates regional ΔR values (Reimer and Reimer, 2001; <http://calib.org/marine/>). We report calibrated ^{14}C ages in years before 1950 Common Era (CE) (Table 2), which result from correcting lab-reported ^{14}C ages to account for variations in atmospheric ^{14}C concentrations over time.

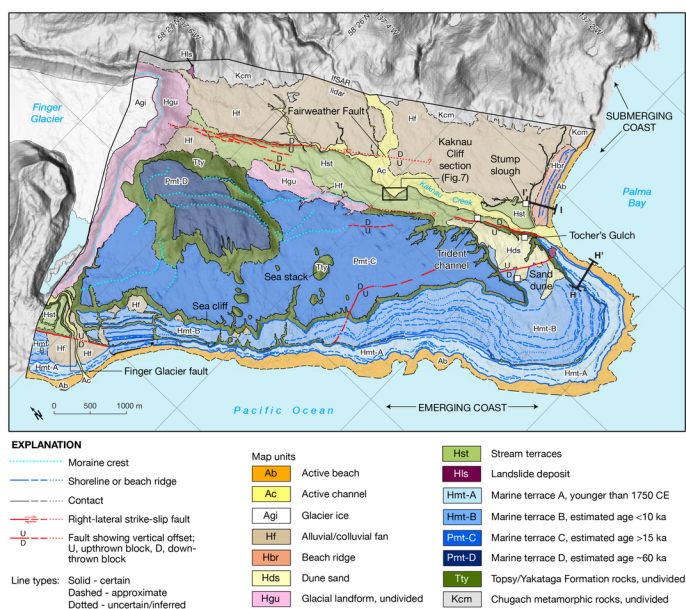


Figure 4. Geomorphic map of Icy Point interpreted from lidar DEM (Witter et al., 2017b). See Figure 2 for location of map within larger coastal context.

4 Results

4.1 Multibeam bathymetry and seismic profiles offshore Icy Point

As it approaches Icy Point from the south, the final 50 km of the Queen Charlotte fault is a subtle, straight seafloor lineament and exhibits no significant bends or steps along strike (Brothers et al., 2020). This section of the fault adjoins the hypocenter of the 1958 Fairweather earthquake and may have initiated the rupture that propagated northwestward onto the Fairweather fault. Although the fault cuts late Holocene basin fill deposited to the east in Palma Bay, the western side of the fault is characterized by elevated topography for >50 km south of Icy Point. Within 10 km of Icy Point, seafloor bathymetry (Figure 2c) and seismic reflection profiles (Figure 5) show contractional structures that underlie the elevated topography west of the

Queen Charlotte fault. The vertical expression of the fault ends within ~1 km offshore Icy Point where it steps 3 km east to the primary strand of the Fairweather fault. Seismic profiles, described next, suggest that the Queen Charlotte fault may bend ~10° to the west and merge with a shallow, 25° east-dipping reverse fault aligned with the Finger Glacier fault mapped onshore (Figure 2c). Offshore, the east-dipping reverse fault forms an up-to-the-northeast scarp that wraps around the southwestern flank of Icy Point; onshore the Finger Glacier fault vertically offsets Terrace B (Hmt-B) and an alluvial fan (Hf) deposited by the Finger Glacier outwash stream (Figure 4). No lateral offset on the Finger Glacier fault has been documented.

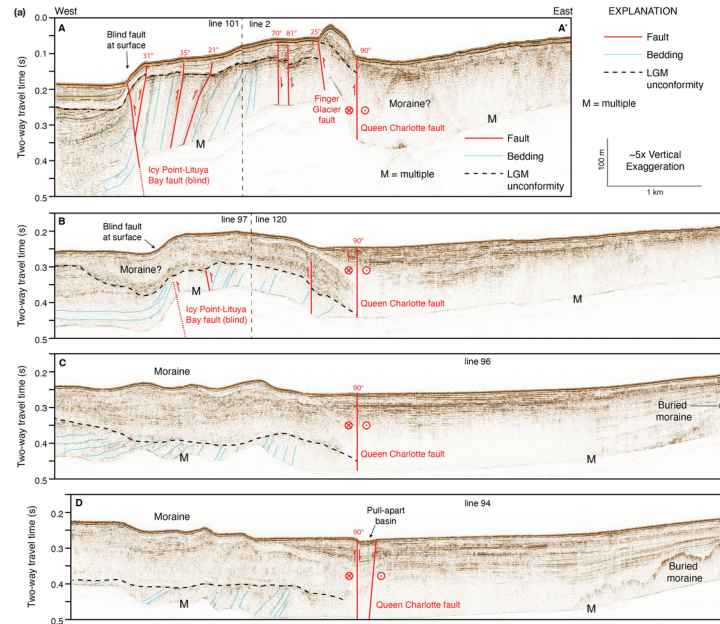


Figure 5. Multichannel seismic profiles acquired south of Icy Point (Balster-Gee et al., 2020); profile locations shown on Figure 2b. (a) Seismic reflection profile A-A' shows the Icy Point-Lituya Bay thrust fault and the Finger Glacier fault, which both dip northeast and offset an erosional unconformity probably formed during the Last Glacial Maximum (LGM). Between the two thrust faults, the LGM unconformity is displaced by bedding-parallel flexural slip reverse faults and by normal faults related to extension above a growing fold. (b) Profile B-B' shows an active fold between the blind Icy Point-Lituya Bay fault on the west and the Queen Charlotte fault on the east. The fold is deformed by bedding-parallel reverse faults and normal faults. (c) In profile C-C' a single, near-vertical strand of the Queen Charlotte fault juxtaposes horizontal strata on the east and possible moraine deposits overlying west-dipping beds below an unconformity on the west. (d) Two strands of the Queen Charlotte fault form a small pull-apart basin in profile D-D'. West-dipping beds below an unconformity indicate folding west of the fault and south of Icy Point. M, sea-floor multiple.

Four multichannel seismic reflection profiles cross the Queen Charlotte fault to the south of Icy Point (Figure 2; Figure 5); these profiles reveal, as one approaches incrementally northward to within 4 km of Icy Point, a growing contractional structure that overlies the buried Icy Point-Lituya Bay fault on the west and is bounded to the east by the Queen Charlotte fault. The contractional structure is defined by the deformation of a prominent unconformity. The unconformity records erosion by advancing ice during the Last Glacial Maximum, (Figure 5), followed by deposition and deformation after the glacial-interglacial transition ca. 17 ka. Beds below the unconformity, which dip to the west, are likely Topsy and Yakataga sediment, which were deposited from late Miocene to Pleistocene and started to be deformed ca. 300,000 years ago based on thermochronometry (Lease et al., 2021). The profiles show that the deformation of Miocene to Pleistocene sediment commenced >15 km south of Icy Point, before the Topsy and Yakataga beds reach the southern end of the restraining bend. Despite the proximity of the northernmost seismic reflection profile to Icy Point

(panel A, Figure 5), the profile shows no expression of the Fairweather fault, which implies that the 3 km right stepover is north of the profile. Although the structures shown in profiles A and B (Figure 5) show the initial contractional strain associated with offshore reverse faults, the uplift of Icy Point is north of the fault step over and bounded on the east by the principal strand of the Fairweather fault, which strikes obliquely to the relative plate motion vector (Figure 6) (Brothers et al., 2020).

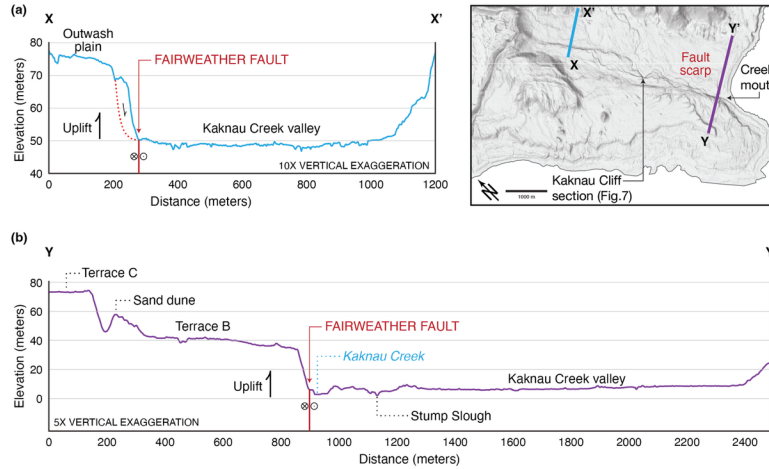


Figure 6. Topographic profiles of the west-side-up principal strand of the Fairweather fault that delineates the western margin of the Kaknau Creek valley. Profile locations shown in map at upper right; red arrows point to 20- to 30-m tall scarp formed by principal fault strand. (a) Tectonic uplift west of the Fairweather fault forms a 20- to 25-m-tall scarp that elevates and isolates outwash plain deposits above active stream channel deposits in the Kaknau Creek valley on the east side of the fault. Secondary scarps near the top of the main fault scarp mark headscarps of large slope failures or secondary faults related to oblique slip. (b) Tectonic uplift elevates marine terraces immediately west of the 25-to-30-m tall Fairweather fault scarp at the mouth of Kaknau Creek. The 1958 fault rupture produced ~ 3 m of right-lateral slip, but no vertical displacement along this profile.

4.2 Timing of deposition and incision in lower Kaknau Creek Valley

Along the western margin of the Kaknau Creek valley, at a site informally called the Kaknau Cliff section, periglacial deposits exposed in ~ 25 -m tall cliffs eroded by the creek (Figure 7) constrain the initial timing of Terrace B emergence and add insight into the vertical component of displacement on the Fairweather fault at Icy Point. Kaknau Creek drains the southwestern corner of the Fairweather Range, and the west side of the valley, near the mouth of Kaknau Creek, is bordered by the active Fairweather fault (Figure 4). The Kaknau Cliff section exposes rhythmically bedded silt and sand deposited in a proglacial lake and cross-bedded sand deposits formed in a proglacial delta. Outwash gravel overlying the lake sediment marks the end of lacustrine deposition (Figure 7). The elevation of the outwash surface (~ 50 m) at the Kaknau Cliff section, >25 m higher than the modern Kaknau Creek channel, implies that the Fairweather fault steps ~ 600 m to the east and forms a 25-m tall, linear escarpment toward the northwest (Figures 4 and 6). Like the modern creek channel, which grades to present sea level, the highest surface of the outwash plain (Hst), based on its elevation and slope, was graded to sea level that formed the highest surface (~ 46 m) of Terrace B.

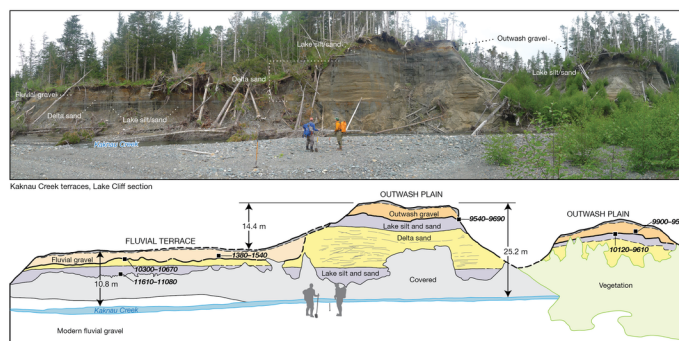


Figure 7. In the lower Kaknau Creek valley, periglacial deposits are preserved in a 25-m-tall cliff that exposes the southwestern bank of the creek that we informally call the Kaknau Cliff section (photo credit: USGS). The Kaknau Cliff section occurs on the uplifted, west side of the Fairweather fault. The deposits include proglacial lake and delta deposits. Radiocarbon ages (Table 1) chronicle a proglacial lake that was extant at $\sim 11,350$ yr BP and persisted until no later than $\sim 9,600$ yr BP. An intervening interval of progradation of clastic deltaic sediment interrupted the fine-grained lake sedimentation. The onset of progradational fluvial outwash gravels, at least by 9,600 yr BP, marks the end of lake sedimentation. The outwash gravels (~ 50 m elevation) grade to the highest surface (~ 46 m elevation) of Terrace B.

The Kaknau Cliff section implies that a lake, which we informally name Kaknau Lake, was dammed behind a terminal moraine formed by ice that advanced down the Kaknau Valley. The lake filled the entire valley and extended across the Fairweather fault. This interpretation is supported by the presence of recessional moraines on Terrace C and radiocarbon ages that indicate the lake formed prior to ~ 11.4 ka and persisted until no later than ~ 9.8 – 10.6 ka (Table 2) (Figure 8). This time frame is consistent with the inference that the lake was dammed behind a terminal moraine formed by ice that advanced down the Kaknau Valley during the Younger Dryas period, 12.9–11.7 ka (Brauer et al., 2008; Rasmussen et al., 2006).

The outwash unit that caps the Kaknau Lake deposits (unit Hst) grades downstream to the highest surface of Terrace B (Figure 4) and, when active, filled the entire Kaknau Creek valley. The age of the outwash provides a maximum-limiting estimate for when the paleo-sea cliff separating Terraces B and C was cut and abandoned. Abandonment occurred after 9.6–10.1 ka, the age of stumps rooted in the deposits of Kaknau Lake and buried by outwash gravel (Figures 7 and 8). Deposition of outwash gravels continued at least until 9.5–9.7 ka, based on the death age of a younger stump buried by outwash (sample #17IP-15-S1, Table 2). Outwash deposition ceased by 5.0–7.0 ka because the outwash gravel predates lower shoreline deposits on Terrace B (discussed below).

The exposure at Kaknau Cliff is the product of lateral stream erosion into a fault scarp. The cliff exposure is not a product of fluvial incision. The exposure is a consequence of lateral erosion by Kaknau Creek into uplifted deposits. The deposits are graded to an uplifted marine platform that only occurs on the west side of the Fairweather fault. Uplift must be at least 25 m because that is the relief of the cliff face.

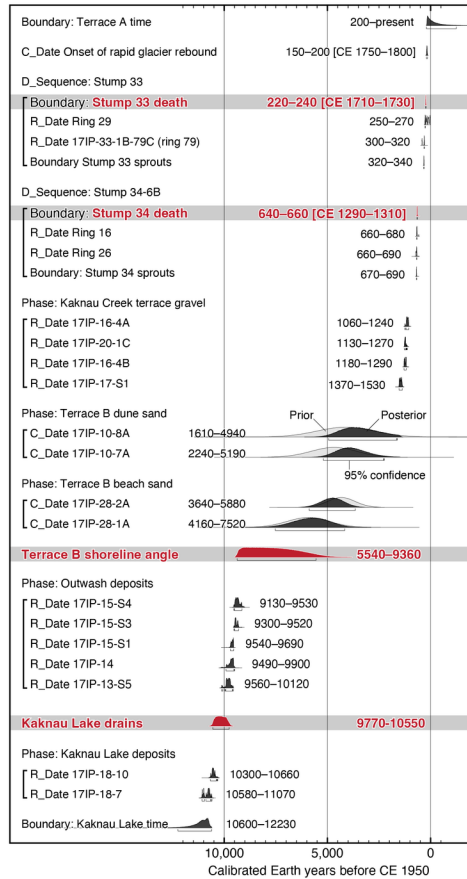


Figure 8. Modeled timing of Kauknau Lake drainage, the age of the Terrace B shoreline angle, and the deaths of sub-fossil stumps 33 and 34 at Stump Slough (Figure 10). Radiocarbon ($n = 15$) and luminescence ($n = 4$) ages inform the model (Witter and Bender, 2021). Red probability density functions (PDFs) show model age ranges (in years before 1950 CE) that span the 95% confidence interval. Light gray PDFs show prior ages for ^{14}C samples (Table 2) and IRSL samples (Table 1); dark gray PDFs show posterior ages. The onset of rapid glacier rebound at 150–200 years before 1950 CE (Mann and Streveler, 2008) is used as a minimum limiting constraint on the death age of stump #33. PDFs are computed using OxCal version 4.4.2 (Bronk Ramsey, 2009; 2023) and the IntCal20 dataset of Reimer et al. (2020) and reported at the 95% confidence interval. The terms Boundary, R_Date, Phase, C_Date, and D_Sequence are commands applied in OxCal model code, which is included in the Appendix.

4.3 Block uplift of Icy Point implied by marine terrace slopes

The slopes of marine terrace surfaces at Icy Point show little evidence for fault-perpendicular tectonic tilting and imply block uplift of the peninsula implicating vertical slip on the Fairweather fault. Slopes measured on lidar topography fall within the range of gradients measured on modern, undeformed shore platforms in central California. Bradley and Griggs (1976) demonstrate that modern platforms slope gently seaward and consist of two sections: an inshore platform (1.1° – 2.3° slope), usually 300–600 m wide, and a slightly flatter offshore platform (0.4° – 1.0°).

We measure the surface slopes of Terraces C and B from profiles of lidar topography depicted in Figure 9 and listed in Table 3. Terrace C, profile H–H', oriented parallel to the Fairweather fault, slopes gently southeast 0.1° – 0.9° . Southwest-facing slopes on Terrace C, profiles I–I' and J–J', oriented perpendicular to the fault, range from 0.9° – 2.3° . At the nose of Icy Point, the flat upper portion of Terrace B slopes 0.8° to

the southeast. Terrace C surface slopes do not necessarily reflect the slope of the underlying erosional marine platform because late Pleistocene glaciers crossed Terrace C and probably modified its surface (Witter et al., 2021). Faults, like the Finger Glacier fault, vertically displace Terraces B and C and impose local, shore-parallel surface deformation. However, all measured surface slopes fall within the range of slopes inherent to undeformed shore platforms, and tectonic tilting of Terraces B and C, if any, likely amounts to less than $\sim 1^\circ$ (Figure 9).

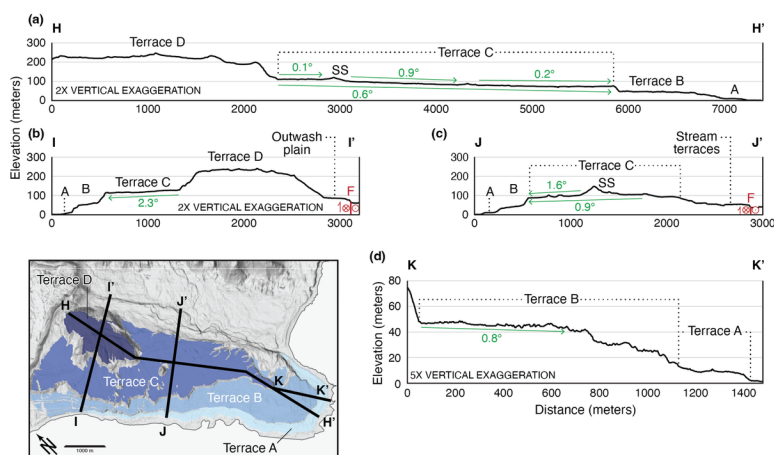


Figure 9. Marine terrace elevation profiles; locations shown on index map at lower left. (a) Elevation profile H–H’ trending northwest showing relative elevation of Terraces D, C, B and A. The riser between Terrace C and B is a paleo sea cliff that marks an interval of relative sea level stasis, when riser height was increased by continued freshening of the base of the riser through coastal erosion. (b) Elevation profile I–I’ trending $\sim 70^\circ\text{E}$, perpendicular across the long axes of Terraces D, C, B and A. The highest Kaknau Creek outwash plain east of Terrace D grades downstream to the highest surface of marine Terrace B. Red letter F marks active strand of Fairweather fault. (c) Elevation profile J–J’ trending $\sim 70^\circ\text{E}$ perpendicular across the long axes of Terraces C, B and A. (d) Elevation profile K–K’ trending $\sim 20^\circ\text{W}$ across Terraces B and A. Arrows in all profiles indicate the direction and length over which terrace slopes were measured on lidar topography (Witter et al., 2017b).

4.4 Little Ice Age coastal geomorphology reflects glacial rebound

Mann and Streveler (2008) reconstructed post-LGM relative sea-level change in Icy Strait and documented a high-sea stand during the LIA and subsequent RSL fall accompanying glacial rebound following 1750 CE. The geomorphology of Terrace A at Icy Point and the ^{14}C ages of coastal landforms backing Palma Bay are consistent with the Icy Strait relative sea-level history. On Terrace A, west of the Fairweather fault, the age (400–30 cal yr BP, Table 2) of a bivalve shell collected within beach sand (Figure 10) implies emergence of the terrace surface within the past few centuries, but broad date uncertainties preclude its use in the age model (Figure 8). The highest beach ridge along the landward edge of Terrace A was formed by the LIA high stand and reaches elevations of 12–14 m (Figures 4 and 10) (Mann and Streveler, 2008).

East of the fault a 12–14 m high, barrier beach ridge fronts the Kaknau Creek valley along the northern shore of Palma Bay. The crests of the beach ridge east of the Fairweather fault has a similar elevation as beach ridge crests backing Terrace A (Figure 10) and both landforms emerged after 1700 CE, based on spruce forest ages and soil development (Mann and Streveler, 2008). We infer that these beach ridges on either side of the Fairweather fault were constructed by ocean waves near the end of the LIA when RSL was ~ 4 m higher than present. The concordance of the beach ridge elevations on either side of Kaknau Creek (Figure 4) indicate that little or no vertical displacement has occurred on the Fairweather fault since the marine transgression that occurred at the height of the LIA, ca. 1750 CE.

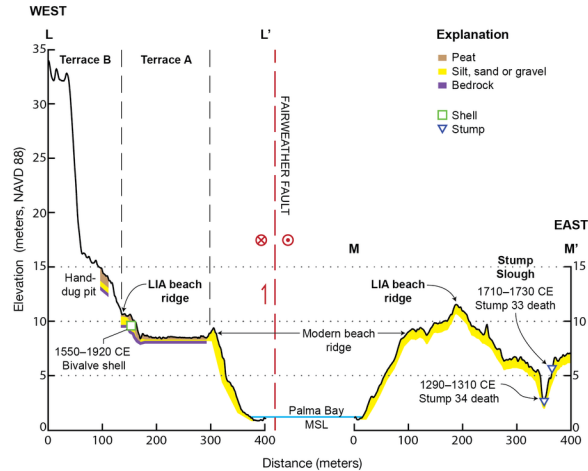


Figure 10. Shore-perpendicular topographic profiles west (left) and east (right) of the Fairweather fault at Icy Point. Profile locations shown in Figure 4. Topographic profile L–L' (left) crosses Terrace A west of the Fairweather fault. Higher emergent shorelines on Terrace B only occur west of the fault (Figure 4). The elevation of the highest beach ridge crest on Terrace A is equivalent to the highest beach ridge crest on the Palma Bay barrier beach located east of the Fairweather fault. Topographic profile M–M' (right) crosses the barrier beach fronting Palma Bay east of the Fairweather fault and shows shorelines uplifted in historic times due to glacial isostatic adjustment ('LIA beach ridge') caused by loss of ice mass in Glacier Bay near the end of the Little Ice Age (LIA). Also shown on profile M–M' is a channel ('Stump Slough') incised into alluvial deposits that records the inception of incision linked to glacial rebound.

Landward of the LIA-age beach ridges east of the Fairweather fault, cutbank exposures in a tributary slough of Kaknau Creek (Stump Slough, Figure 10) record centuries of alluvial flooding that drowned and buried spruce trees in a coastal forest. Channel incision accompanying post-LIA isostatic rebound has exposed growth-position, subfossil trees. The stratigraphically lowest sub-fossil trees exposed in Stump Slough died near the turn of the 13th century between 1290 and 1310 CE. Typically, the outer rings of the stumps were too narrow to provide enough material for ¹⁴C dating, so we sampled larger interior rings. To estimate the time the tree died, we used a Bayesian model that incorporates ¹⁴C dates of the 16th and 26th rings sampled from stump #34 exhumed in the slough channel (Table 2, Figure 8). Alluvial sediment buried another stand of trees at 1710–1730 CE, entombed 4 m higher in the cutbank, based on dating rings 29 and 79 sampled from stump #33 (Table 2, Figure 8). The higher trees lie ~1 m below the top of the cutbank, which marks the level of highest alluvial aggradation. After 1730 CE, channel incision exposed the buried forest stratigraphy in the slough cutbank (Figure 10).

We interpret the Terrace A geomorphology and stratigraphy of Stump Slough in the context of RSL fluctuations caused by isostatic adjustment during the LIA (Mann and Streveler, 2008). The LIA began around 1300 CE, when ice advanced down Glacier Bay and into Icy Strait (McKenzie and Goldthwait, 1971) causing regional isostatic depression and a high-sea stand (Motyka, 2003; Larsen et al., 2005). We attribute the highest beach ridge crests on Terrace A and in the barrier complex facing Palma Bay as shorelines recording the LIA high-sea stand (Figure 10). Regional isostatic rebound and RSL fall initiated in 1750–1800 CE when the retreat of marine-based ice in Glacier Bay began to accelerate. Along the coast of Palma Bay, the stratigraphy exposed in Stump Slough records the drowning of spruce trees in 1290–1310 CE caused by RSL rise in the beginning of the LIA, which raised the base level of Kaknau Creek. The highest buried stumps in the profile show that the creek continued to drown trees as late as 1710–1730 CE—just a few decades before the sudden retreat of Glacier Bay ice caused isostatic rebound.

4.5 Terrace B: A sequence of uplifted Holocene shorelines

Terrace B is a composite, time-transgressive surface that steepens toward the sea and is etched by 9 to 12 shorelines. These shorelines, mapped on lidar DEMs and verified in the field, create a stair-stepped profile in the lower half of Terrace B and represent paleo-sea cliff and shore platform junctions (Trenhaile, 1972; Kelsey, 2015). Each higher, older shoreline has the same general planform as the one below (Figure 11). The highest shoreline follows the base of the sea cliff separating Terraces B and C. The shorelines record episodes of sudden shoreline emergence along an uplifting coast west of the Fairweather fault (Figures 9 and 11). In the field, we confirmed that these shorelines (sea-level indicators) mark the paleo-sea cliff and shore platform junctions (shoreline angles) and provide an indicative meaning of approximately mean high water (MHW) (e.g., Kelsey, 2015).

The longshore preservation of individual shorelines varies across Terrace B. Near Icy Point, the southern part of Terrace B preserves 9–12 shorelines that climb to a maximum elevation of about 50 m. We map these shorelines as continuous landforms based on their geomorphic expression and elevation (Figure 11). In the central part of Terrace B, few shorelines are preserved, and a ~40 m high uplifted sea cliff, probably eroded during the LIA, backs Terrace A. The northern extent of Terrace B includes 9–10 shorelines expressed as prominent paleo-sea cliffs and more subtle shore-parallel, slope breaks and ridges. The oldest and highest shorelines along the northern part exceed the elevation of the highest shoreline in the southern part of Terrace B and reach a maximum elevation of ~70 m (Figure 9), where the Finger Glacier fault vertically displaces Terrace B (Figure 4).

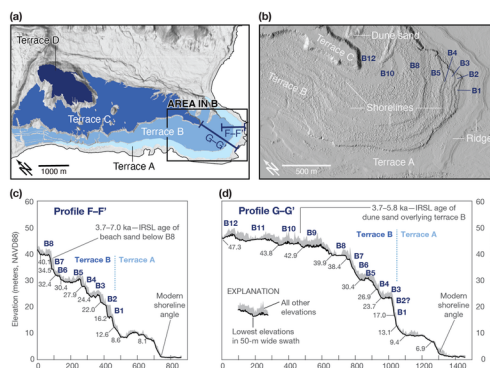


Figure 11. (a) Map of Icy Point marine terraces showing area of lidar topography (Witter et al., 2017b) featured in (b) and the locations of two elevation profiles across Terraces A and B. (b) Lidar topographic map of the southern-most nose of Icy Point. Shore-parallel beach ridges visible on the lowest surface, Terrace A, evidence gradual, ongoing glacial isostatic rebound following the LIA. Erosional beach scarps delineate shorelines (B1, B2, etc.) beveled into Terrace B and elevated by uplift during repeated earthquakes. (c) Topographic profile F–F’ plotting the lowest lidar-measured elevations (black line) along a 50-m wide swath shown in map (a); all other elevations along the swath plotted in gray. Numbers below the profile indicate shoreline angle elevation in meters (NAVD 88). Beach sand below shoreline B8 dates to 3.7–7.0 ka. (d) Topographic profile G–G’ extending from the modern shoreline to the ancient seacliff separating Terrace B and Terrace C. Dune sand covering the highest shorelines dates to 3.7–5.8 ka.

4.6 Age of the paleo-seacliff separating Terraces B and C

We dated coastal landforms to estimate the age of the 30-to-60-m-tall paleo-sea-cliff that separates Terrace B from the older and topographically higher Terrace C (Figures 4 and 9). On the highest surface at the southern end of Terrace B, at an elevation of ~56 m near the foot of the paleo-sea cliff, we excavated a ~2-m-deep pit in an aeolian sand dune (Sand dune, Figure 4). The parabolic shape of the dunes, with steepest aspect toward the southwest, suggest katabatic winds blowing off glaciers to the northeast mobilized beach sand and deposited it on emergent marine terraces. At depths of 1.05 and 1.42 m in the pit we sampled aeolian sand for IRSL age determinations on feldspar grains to estimate the last time the dune sand had

been exposed to light. The shallower sample has an IRSL age of 4.18 ± 1.39 ka and the deeper sample has an IRSL age of 4.74 ± 1.10 ka (Table 1).

We also sampled beach sand from an exposure of marine terrace sediment below Terrace B shoreline B8 at an elevation of ~ 35 m near the top of a steep-sided ravine (Tocher’s Gulch, Figures 4 and 11). The beach sand deposit was ~ 4 m thick above Topsy Formation bedrock and we sampled at depths of 2.70 m and 3.89 m below the terrace surface. The shallower sample has an IRSL age of 4.39 ± 0.66 ka and the deeper sample has an IRSL age of 5.99 ± 1.02 ka (Table 1). From these ages and their uncertainties we infer that beach processes began depositing sand before 5.0–7.0 ka and terrace emergence occurred sometime after 3.7–5.0 ka.

The IRSL ages of separate landforms provide independent minimum estimates for the time of abandonment of the highest shoreline angle that separates Terrace B from Terrace C (Figures 4 and 12). The highest shoreline angle was abandoned before 5.0–7.0 ka because beach sand exposed in Tocher’s Gulch, at an elevation more than 20 m below the highest shoreline angle, was active at this time. A second minimum age for the emergence of the paleo-sea cliff comes from the age of aeolian sand, 3.6–5.8 ka, which advanced over Terrace B after its highest shoreline was abandoned. At a human occupation site near Tocher’s Gulch, charcoal at the base of aeolian sand dated to 4.8–5.2 ka (Crowell et al., 2013). Considering the IRSL data and the coastal landforms from which the samples come, the minimum age of 5.0–7.0 indicated by beach sand more closely limits the time of abandonment (Figure 8).

To estimate the age of the Terrace B shoreline angle we use a numerical model (OxCal, v4.4.2; Bronk Ramsey, 2009; 2023) to compute the 95% age range (probability density function) based on maximum and minimum age constraints. Radiocarbon ages from outwash gravel graded to the highest Terrace B shoreline provide maximum age constraints that range from 9.1 to 10.1 ka. Minimum age constraints come from younger beach deposits, estimated to range from 5.0 to 7.0 ka, that post-date the cutting of the Terrace B shoreline angle. Given these age constraints, the shoreline angle at the top of Terrace B was cut between 5.5 and 9.4 ka (Figure 8).

4.7 Reconstructing the tectonic component of relative sea-level change at Icy Point

Profoundly different Holocene RSL histories occur on either side of the Fairweather fault. Although geomorphic features left by the LIA sea-level highstand do not vary across the fault, tectonic features differ markedly across the fault. Based on these differences evident within hundreds of meters of the Fairweather fault, we show that the different RSL histories can be explained by tectonic uplift west of the Fairweather fault (Figure 12).

In Icy Strait, 30 km east of the Fairweather fault, RSL change fluctuated from 4.1 ± 1 m below present sea level at 6.9–7.2 ka to its present elevation, including the Little Ice Age high stand that registered ~ 4 m above present for the several centuries ending by 1750–1800 CE (Mann and Streveler, 2008) (Figure 12). Although Mann and Streveler (2008) assume that tectonic effects were unimportant in the RSL history in Icy Strait east of the Fairweather fault, in fact their reconstruction incorporates all of the varied factors affecting RSL: eustasy, isostasy, tectonism, local, and other processes (Shennan et al., 2012). We adopt their assumptions and utilize their Icy Strait RSL reconstruction 30 km northeast along the open-ocean coast from Icy Strait to the east side of the Fairweather fault at Palma Bay (Figure 1). Several observations support this extension: 1) relatively low thermochron ages for rock samples at Palma Bay sites east of the Fairweather fault indicate low rock uplift (Lease et al., 2021); 2) the absence of marine terraces along the coast of Palma Bay; 3) low seismicity and the lack of mapped convergent structures east of the Fairweather fault at the latitude of Icy Point; and 4) geodetic data that indicate that fault-normal strain can be accommodated by reverse faults west of the Fairweather fault.

In contrast to the coastline east of the Fairweather fault, RSL at Icy Point has fallen 42.3 ± 2.1 m during the Holocene based on the elevation of the Terrace B shoreline angle relative to the modern shoreline (Figure 12; Table 4). We reconstruct RSL change at Icy Point by comparing the heights of the Terrace B shoreline angle with its modern equivalent. The height of the Terrace B shoreline angle was estimated by subtracting

the thickness of terrace sediment (3 ± 1 m), approximated from field exposures and pits, from the elevation of the inner edge of terrace B at the base of the sea cliff leading up to Terrace C. We determined the mean elevation (47.3 ± 1.7 m) of the Terrace B inner edge by tabulating the elevation of the sharpest inflection at the base of the sea cliff in 25 lidar profiles (Table 4). The elevation of the modern shoreline angle (2.0 ± 0.8 m, NAVD 88 datum) was determined from measurements of 50 lidar profiles along the inner edge of the shore platform. We subtract the Terrace B shoreline angle from the modern shoreline angle (Table 4) to estimate the change in RSL at Icy Point (-42.3 ± 2.1 m) since the original formation of Terrace B between 5.5–9.4 ka.

To evaluate the contribution of tectonic processes to RSL changes at Icy Point, we assess the difference between Holocene RSL change on either side of the Fairweather fault (Figure 12), including all factors that affect RSL change (Shennan et al., 2012; Shennan, 2015). We assume that, within errors of the methods we use and those of Mann and Streveler (2008), the contributions of eustacy, isostasy, and local tidal effects to RSL change do not vary directly east and west of the Fairweather fault at Icy Point. However, the tectonic contribution to RSL change varies substantially across the fault. Therefore, taking the difference in Holocene RSL change across the fault results in a measure of the tectonic contribution of RSL.

To assess the difference in RSL change across the Fairweather fault, we first reconstruct Holocene RSL curves for Icy Point and Palma Bay (Figure 12). We estimate that since the formation of the Terrace B shoreline angle at Icy Point between 5.5–9.4 ka, RSL has fallen dramatically, equaling -42.3 ± 2.1 m (Table 4); whereas, based on reconstructions along Icy Strait, including Palma Bay directly east of the Fairweather fault, RSL has risen $+4.1 \pm 1.0$ m since 6.9–7.2 ka (Mann and Streveler, 2008). The difference in RSL change across the Fairweather fault indicates that the tectonic contribution to RSL change at Icy Point is -46.4 ± 2.4 m (Table 4, Figure 12). The rate of RSL fall at Icy Point, -6.8 ± 2.2 m/ky, is the quotient of the tectonic contribution to RSL change divided by the age of the Terrace B shoreline angle (see Figure 4). We attribute this substantial rate of RSL fall at Icy Point to tectonic rock uplift since the formation of Terrace B at the rate of 6.8 ± 2.2 m/ky (4.6 to 9.0 mm/yr).

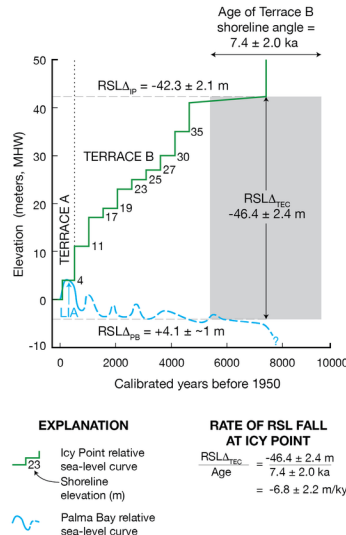


Figure 12. Relative sea level (RSL) curves for Icy Point (this study) and Palma Bay (Mann and Streveler, 2008)—two sites separated by the Fairweather fault. Both sea level curves are tied to the present (0 yr BP) and defined by shoreline features referenced to the elevation of the modern shoreline angle, which approximates Mean High Water (MHW). The greatest contribution to uncertainty in these curves is the timing of deceleration in the rate of eustatic sea level rise in the early Holocene, which allowed local processes to exert greater influence on RSL change at Icy Point. The time when eustatic sea level ceased to be the

dominant control on RSL is best approximated by the age of abandonment of the Terrace B paleo sea cliff (see text) at 7.4 ± 1.2 ka. The stair-step pattern of the Icy Point RSL curve (green) reflects shoreline features on Terrace B interpreted as evidence for repeated coseismic uplift that contributed to -42.3 ± 2.1 m of RSL change at Icy Point ($RSL\Delta_{IP}$). In contrast, the RSL curve in Palma Bay (blue) shows a history of $+4.1 \pm \sim 1$ m of RSL change ($RSL\Delta_{PB}$) in response to fluctuating ice loads in neighboring Icy Strait and Glacier Bay (Mann and Streveler, 2008). The tectonic component of RSL change ($RSL\Delta_{TEC}$), -46.4 ± 2.4 m, is the difference between the two RSL curves separated by the Fairweather fault ($RSL\Delta_{TEC} = RSL\Delta_{IP} - RSL\Delta_{PB}$, Table 4).

5 Discussion

Our findings suggest that the Icy Point, located at the southern end of a restraining double bend in the Fairweather fault, episodically emerged above sea level during repeated fault ruptures that coseismically raised the coast. The faults bounding the peninsula that accommodated the uplift include the Fairweather fault to the east and both the Icy Point-Lituya Bay reverse fault and the Finger Glacier reverse fault to the west. We attribute -46.4 ± 2.4 m of relative sea level fall over the past 7.4 ± 2.0 ka at Icy Point to tectonic vertical land-level change, which implies Holocene rock uplift rates of 4.6 to 9.0 mm/yr. This Holocene rate is consistent with a thermochronometric record that implies Quaternary rock exhumation rates of 5–10 km/m.y. and right-lateral strike-slip rates of 45–49 mm/yr along the Fairweather fault (Lease et al., 2021). Using the slip rate and vertical displacement rate observations we discuss the possible plate-boundary fault geometries and rupture kinematics consistent with our observations in the vicinity of Icy Point.

5.1 Mechanism of late Holocene rock uplift at Icy Point

The 30-to-60-m-tall paleo-sea cliff separating Terrace B from Terrace C and the broad beveled platform fronting the paleo sea cliff (Figure 9), both imply sustained erosion during rapid post-Last Glacial Maximum sea level rise driven by eustasy in the early Holocene. Rapid tectonic uplift at Icy Point may have kept pace with eustatic sea level rise, resulting in very little change in RSL for several millennia. Mann (1986; p. 247) inferred just such a scenario: “Furthermore, wide bedrock terraces on a tectonically rising coast are thought to be cut during periods when rising eustatic sea level keeps pace with uplift (Bradley and Griggs, 1976).” However, after the decay of the large ice sheets ~ 7 ka, global eustatic sea-level rise decelerated (Fleming et al., 1998) and tectonic uplift at Icy Point outpaced other effects, causing RSL to fall. Terrace emergence resulted from a prolonged interval of marine regression, punctuated by at least 9–12 episodes of coseismic uplift that have left a descending series of paleo-shorelines marked by erosional scarps and barrier beaches across the lower extent of Terrace B (Figure 11).

On tectonically active coasts, tectonic uplift, frequently coseismic, can raise shorelines so that they become stranded above sea level (Wellman, 1969, Ota et al., 1991; Nelson and Manley 1992, McSaveney et al., 2006; Berryman et al., 2018). For example, Turakirae Head on the south end of the North Island of New Zealand features four prominent beach ridges that are vertically separated from each other by 3.4–7.1 m (Aston, 1912; Wellman, 1969; McSaveney et al., 2006). Little et al. (2009) inferred that the elevation difference of adjacent raised ridges at Turakirae Head is a measure of coseismic uplift that caused the stranding of successively higher-elevation shorelines.

In a similar way, we infer that coseismic uplift stranded shorelines at Icy Point. Three observations support this inference. First, as discussed above, the RSL history differs markedly on either side of the Fairweather fault, and we infer that the difference reflects repeated coseismic uplift on the west side of the fault, while little or no tectonic uplift occurred over the same interval east of the fault. Second, the geologic structure of the Icy Point peninsula provides an uplift mechanism (Figure 13): the Icy Point peninsula is bounded on the east by the Fairweather fault, which has a component of west-side-up throw; and Icy Point is in the uplifted hanging wall of the Icy Point-Lituya Bay thrust fault, which bounds the peninsula on the west. Third, the relatively narrow width (<10 km) separating the two faults, which bound the uplift, suggest permanent strain on shallow crustal structures. A series of coseismic uplift events accommodated by these two bounding faults can account for the observed RSL fall over the past 5.5–9.4 ky at Icy Point.

The nearfield kinematics within the restraining double bend of the southern Fairweather fault resemble simple, uniformly uplifted, “pop-up” structures bound by steep ($>70^\circ$) faults demonstrated in analog models of transpressive systems with 15° – 30° convergence angles (Casas et al., 2001). The tilt of Terrace B does not exceed typical shoreline gradients and implies uniform or block-like uplift at Icy Point (Figure 2c). Uniform uplift of a block can be explained kinematically by 1) deformation related to a back-thrusts off the Icy Point-Lituya Bay fault (Pratt et al., 2015), or 2) a shallow (<1 km) depth of the buried tip of the Icy Point-Lituya Bay fault offshore. Better constraints on fault geometries may resolve the kinematics of deformation at Icy Point in greater detail, as both explanations above are consistent with the expression of the faulting in Figure 5a. Comparison with other transpressive, strike-slip fault systems and analog modeling also may lead to insights about the nearfield kinematics along the southern Fairweather fault (e.g., Cowgill et al., 2004; Mann, 2007; Toeneboehn et al., 2018; Benowitz et al., 2021).

5.2 A history of earthquakes that sustain extreme uplift rates at Icy Point

The descending series of 9–12 abandoned shorelines present on Terrace B records repeated episodes of vertical displacement (Figure 11). Field measurements of the vertical step in topography that marked each shoreline ranged from 3 to 5 m (Figure 12). The along shore continuity and step-like geometry indicate sudden vertical displacements, which we attribute to coseismic uplift during earthquakes. The position of the shorelines in the hanging walls of two active reverse faults, the Finger Glacier fault and the offshore Icy Point-Lituya Bay fault provide further support for a coseismic origin. The highest shoreline angle of Terrace B formed 5.5–9.4 ka. Therefore, if each of the 9–12 Terrace B shorelines on Icy Point record coseismic vertical displacement, then the peninsula jerked upwards during a major earthquake every 460–1040 years. This recurrence interval is a maximum estimate because evidence for coseismic uplift events with smaller vertical displacements may not be preserved (or detected) in the coastal geomorphology.

Based on measured elevations of these abandoned shorelines (Figure 12), individual instances of coseismic uplift varied from 3–5 m, with an average of 3.4 m. We infer that coseismic uplift preserves these abandoned shorelines, isolating the former active shoreline and therein triggering formation of a new active shoreline and beach through wave swash processes. The average vertical separation of 3.4 m likely is a maximum, because some earthquakes may have produced <1 m of uplift insufficient to isolate and preserve a shoreline (Pratt et al., 2015), or the shoreline was obscured by beach deposits and not evident in the terrace geomorphology. Further, these values exceed average displacements for reverse and oblique reverse mechanism earthquakes in the historic record (Moss et al., 2022), suggesting the uplift is either focused at Icy Point (a region of maximum uplift) or each shoreline represents one or more events.

Our results imply that past earthquakes accompanied by vertical displacement sufficient to raise and preserve marine shorelines involved a different faulting mechanism than the 1958 M_w 7.8 Fairweather earthquake. The 1958 earthquake was predominantly strike-slip and caused no observable uplift at Icy Point. Moreover, the concordance of beach ridge crest elevations on Terrace A and LIA barrier beaches both east and west of the Fairweather fault requires a common history of RSL fall and rules out measurable post-LIA differential uplift. Our geomorphic mapping (Figure 4) shows that the Fairweather fault also delineates a structural eastern boundary of marine and fluvial terrace uplift at Icy Point. Because our analysis of Icy Point terrace slopes (Figure 9) argues for uplift with minimal accumulated tectonic tilt, we infer that movement on both the Fairweather fault and structurally linked reverse faults (e.g., the Icy Point-Lituya Bay thrust fault) (Figure 2 and 10) produces the morphology of Icy Point abandoned shorelines.

5.3 Strain partitioning at the plate-boundary restraining double bend

Icy Point is at the south end of a restraining double bend in Earth’s fastest-slipping, transform plate boundary fault system (Witter et al., 2021). Restraining bends in strike-slip fault systems focus areas of high rock uplift, and the fault geometries that drive uplift at restraining bends are diverse (Cowgill et al., 2004; Cunningham and Mann, 2007; Mann, 2007). Inherited structural complexity is a major determinant in the fault geometry; for example, at restraining bends along the San Andreas fault (Anderson, 1990; 1994; Burgmann et al., 1994; Cowgill et al., 2004; Spotila et al., 2001; Spotila et al., 2007). For the restraining bend along the Fairweather

fault north of Icy Point, the contrast in rock types and in rheology across the plate boundary influences the resultant tectonic structures (Molnar and Dayem 2010; Fitzgerald et al., 2014; ten Brink et al., 2018). Amphibolite-facies gneiss and gabbro in the Fairweather Range, east of the restraining double bend, provide a buttress and focus upper-crustal deformation to the west side of the restraining fault bend in the weaker sedimentary rocks of the Cretaceous-Cenozoic Yakutat block (Lease et al., 2021).

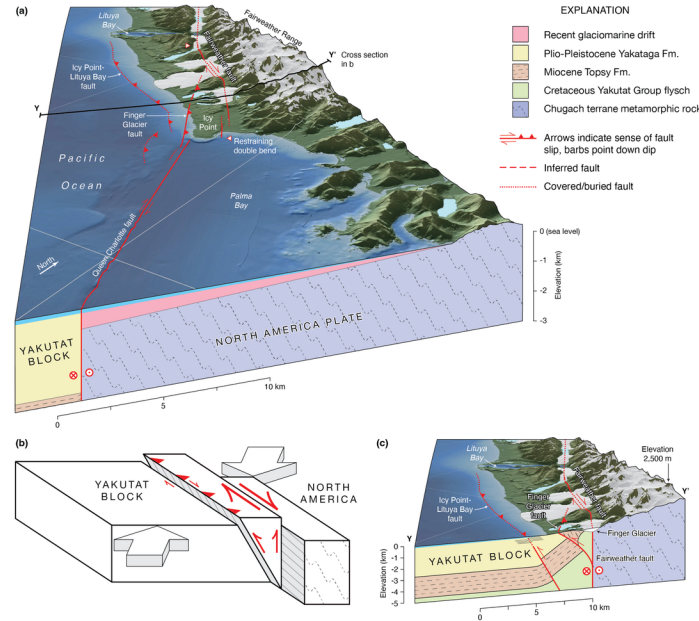


Figure 13. (a) Oblique view looking to the northwest where the offshore Queen Charlotte fault steps 3 km east to the Fairweather fault. Data sources for onshore and offshore elevation models described in Figure 2 caption. The location of the southern termination of the offshore Icy Point-Lituya Bay reverse fault is inferred from seismic profiles shown in Figure 5. (b) Conceptual block model depicting transpression, or oblique contraction, in a right-lateral transform plate boundary. Arrows indicate relative fault slip rates (after Wesnousky, 2005). (c) Our tectonic model for the restraining double bend along the southern Fairweather fault consists of a one-sided, positive flower structure that includes the steeply dipping Fairweather fault to the east of Icy Point and two reverse faults, the Icy Point-Lituya Bay and Finger Glacier faults. The Icy Point-Lituya Bay fault splays off the Fairweather fault at seismogenic depths; the Finger Glacier thrust fault is a shallow secondary structure. The Icy Point-Lituya Bay fault and the Fairweather fault accommodate oblique contraction where the Yakutat block obliquely collides into North America.

Uplift and contraction at Icy Point are accommodated by faults with reverse slip, strike slip, and oblique-slip behaviors. Because of its near-vertical dip (Tocher, 1960; Doser and Lomas, 2010), the Fairweather fault does not accommodate contraction. Shortening along the restraining double bend is accommodated by reverse faults, most notably the offshore Icy Point-Lituya Bay fault. Because the Icy Point peninsula is uniformly uplifted (Figure 9b and c), there must be vertical displacement on the Fairweather fault during some earthquakes. Kinematically, this requires that some earthquakes on the Fairweather fault involve oblique slip. Alternatively (or, in addition), the Fairweather fault on the east side of the Icy Point peninsula may slip in a bimodal fashion during independent strike-slip and vertical-slip fault ruptures (e.g., Barnhart et al., 2015).

Several observations guide our conceptual model of fault-driven deformation west of the restraining bend at Icy Point. First, the obliquity between the strike of the Fairweather fault and Yakutat-North America plate motion ($22^\circ \pm 8^\circ$; Brothers et al., 2020), provides the setting for the restraining double bend and accounts

for the topographic relief of the contractional foothills (Fairweather and Yakutat foothills) to the west of the Fairweather fault. Second, at Icy Point, uplifted Holocene shorelines on Terrace B imply an earthquake cadence that averages 3.4 m of coseismic uplift every 460–1040 yrs. Third, the Fairweather fault on the east margin of Icy Point has accommodated at least 25 m of vertical, west-side-up displacement in the past 10 ky based on uplifted periglacial and outwash deposits at the Kaknau Cliff section. Finally, because the 1958 M_w 7.8 Fairweather earthquake was predominantly strike slip and caused no detectable vertical displacement at Icy Point, there must be a set of earthquakes with different rupture modes than the 1958-type earthquake because, every 460–1040 years, at least one plate boundary earthquake causes measurable, \sim 3.4 m, coseismic uplift of the Icy Point peninsula. By comparison, the average recurrence interval for predominantly strike-slip earthquakes on the Fairweather fault like the 1958 event (3.5 m per event) is <100 years (Witter et al., 2021).

5.4 A one-sided, positive flower structure fault model

A conceptual fault model of deformation at the restraining double bend that accommodates a fast-slipping transform plate boundary with extraordinary rock uplift rates at Icy Point is one in which the principal strand of the Fairweather fault forms the eastern margin of a “one-sided,” positive flower structure (Figure 13) (Woodcock and Fischer, 1986; Bruhn et al., 2004; Pavlis et al., 2004). The structure initiates 1–2 km south of Icy Point, where the offshore Queen Charlotte fault steps 3 km east to the onshore Fairweather fault, undergoes a $\sim 20^\circ$ bend, and ends in the north near Lituya Bay (Witter et al., 2021). The Queen Charlotte fault may merge with the east-dipping Finger Glacier fault as implied by offshore seismic profiles (Figure 5). Transpression imposed by the $>20^\circ$ obliquity between the strike of the Fairweather fault and Yakutat-North America plate motion (Brothers et al., 2020) drives the asymmetrical flower structure at Icy Point; contraction is accommodated primarily on the Icy Point-Lituya Bay reverse fault that splays off the Fairweather fault at seismogenic depths (<20 km depth, Table 5). The simple fault model depicted in Figure 13 does not explain the complex dynamics required by the continual lateral advection of crust through the corner of a stationary restraining bend.

The asymmetrical flower structure model accommodates shortening between crustal slivers along the northeastern edge of the Yakutat block (Bruhn et al., 2004; Pavlis et al., 2004). The model we propose is consistent with geodetic block models that place convergence on reverse faults west of the Fairweather fault (Elliott et al., 2010; Elliott and Freymueller, 2020) and differs from models of slip partitioning that infer substantial convergence on unidentified structures east of the fault under the Fairweather Range (McAleer et al., 2009). We present an alternative model that infers that the strain-weakened edge of the Yakutat block abuts the strong crystalline core of the Fairweather Range and that high rates of horizontal and vertical deformation are localized west of the Fairweather fault. Our contention that the near vertical Fairweather fault accommodates substantial vertical slip is similar to models of vertical extrusion attributed to oblique convergence along the sub-vertical Denali fault (Benowitz et al., 2022).

5.5 Fault rupture scenarios accommodating oblique contraction

Several fault rupture scenarios could account for the uplift rates recorded at Icy Point in the Holocene. A ‘joint rupture’ scenario involves the simultaneous ruptures of the Fairweather fault and the offshore Icy Point-Lituya Bay fault. In this scenario, coseismic slip on the Fairweather fault at depth propagates upward and intersects the Icy Point-Lituya Bay fault where a component of slip splays off the primary strand of the Fairweather fault. Slip is partitioned into reverse slip on the blind Icy Point-Lituya Bay fault and vertical- or oblique-slip on the Fairweather fault. This scenario consists of joint rupture of both faults and causes uplift of the Icy Point peninsula. There may be seaward (westward) tilting during uplift because a blind reverse fault like the Icy Point-Lituya Bay fault can exhibit diminishing slip towards the tip, promoting more uplift above the location where the reverse fault splays off the Fairweather fault. However, the measured westward slopes of terraces B and C (Figure 9) do not exceed seaward gradients typically cut by shore platform formation along the coast.

An alternative to joint rupture of both faults is a scenario that invokes independent ruptures of the Fairweather fault and the Icy Point-Lituya Bay fault. This ‘independent rupture’ scenario entails vertical- or

oblique-slip on the Fairweather fault that relieves a substantial component of vertical strain, and subsequent reverse slip on the offshore, blind Icy Point-Lituya Bay fault that relieves strain oriented perpendicular to the plate boundary. The oblique-slip events on the Fairweather fault must be balanced by events with sufficient horizontal slip that eventually sum to the long-term fault slip rate. The oblique-convergent ruptures that caused the 2010 and 2021 Haiti earthquakes offer comparative analogs of complex, serial ruptures along an oblique contractional fault system involving strike-slip and reverse faults (Hayes et al., 2010; Okuwaki and Fan, 2022).

Both earthquake scenarios require that the Fairweather fault is an oblique-slip fault at seismogenic depths and accommodates both vertical and horizontal slip. The vertical component of slip is recorded in the northern two seismic profiles (panels A and B) in Figure 5, which mark the commencement of growth of the “Fairweather foothills.” The Fairweather foothills, and the Yakutat foothills to the north, record contraction of crustal slivers along the northeastern edge of the Yakutat block (Bruhn et al., 2004; Pavlis et al., 2004; Elliott and Freymueller, 2020). Horizontal shortening occurs through slip on the Icy Point-Lituya Bay and Yakutat faults; rock uplift is the result of the vertical component of slip on the Fairweather fault and reverse faults that define the crustal slivers to the west.

Multiple earthquake scenarios are supported by observations of coseismic slip in other transpressional fault systems that change the Coulomb stress on adjacent strike-slip and reverse faults and either promote or inhibit failure (Lin and Stein, 2004). Along the Fairweather fault, rupture of adjacent reverse faults can promote failure along strike-slip faults. For example, the 1899 M_w 8.1 Yakutat Bay earthquake promoted failure on the Fairweather fault at the northwestern section of the 1958 rupture (Rollins et al., 2020) and blind thrust faults promote failure over broad areas of the overlying crust (Lin and Stein, 2004). Rupture of the Fairweather fault also likely promoted failure on reverse faults northwest of Yakutat Bay (Rollins et al., 2020). For comparison, the M_w 7.9 San Andreas fault earthquake of 1857 promoted failure on nearby thrust systems including the Coalinga and White Wolf reverse faults (Lin and Stein, 2004). The M_w 7.9, 2002 Denali fault earthquake and its foreshock, the M_w 6.7 Nenana Mountain earthquake, provide an example of stress transfer from the Nenana Mountain strike-slip foreshock to the hypocentral area of the Denali earthquake mainshock (Anderson and Ji, 2003). Stress transfer from the Nenana Mountain earthquake promoted complex reverse-oblique and strike-slip ruptures on the Susitna Glacier thrust and Denali faults, respectively (Eberhart-Phillips et al., 2003; and Aagaard et al., 2004). In this context, Coulomb stress changes resulting from complex oblique-slip, reverse, and strike-slip fault ruptures along the restraining double bend north of Icy Point may periodically promote vertical slip on the Fairweather fault.

5.6 Earthquake source parameters for the offshore Icy Point-Lituya Bay thrust fault

Slip on the offshore Icy Point-Lituya Bay thrust fault represents a source of earthquakes and tsunamis along the Gulf of Alaska coast in addition to strike-slip ruptures along the Fairweather fault. The 1958 M_w 7.8 Fairweather earthquake primarily relieved shear strain parallel to the plate boundary. Published slip rates for the Fairweather fault (46–58 mm/yr) imply average recurrence intervals of 60–140 years for $M_w > 7$ strike-slip earthquakes (Plafker et al., 1978; Witter et al., 2021). This investigation derives fault source parameters for repeated Holocene ruptures on the Icy Point-Lituya Bay thrust fault that relieved fault-normal strain, caused coseismic uplift at Icy Point, and included substantial vertical displacement on the Fairweather fault. Moreover, rupture of offshore thrust faults may explain large tsunamis in Lituya Bay in 1853–1854, ca. 1874, and ca. 1899 (Miller 1960).

Reverse slip on the Icy Point-Lituya Bay thrust fault evidenced by uplifted Holocene terraces at Icy Point occur no more than every 460–1040 years. Assuming a simple fault geometry for a thrust or reverse fault striking subparallel to the plate boundary and dipping between 45°–75° and coseismic uplift of 3–5 m per earthquake based on terrace riser heights, we estimate that the slip during past events on the Icy Point-Lituya Bay fault ranged between 3.1 and 10 m (Table 5). Because the reverse fault is blind, its dip is unknown. Shallower fault dips (30°–45°) are most consistent with geodetic estimates of fault-normal rates of motion (5–14 mm/yr of shortening) perpendicular to the plate boundary (Table 5) (Elliott and Freymueller, 2020); steeper dips (60°–75°) are required if the reverse fault slips off the Fairweather fault at seismogenic

depths (10–16 km). Hypothetical ruptures of the Icy Point-Lituya Bay fault with rupture lengths equal to or exceeding the distance between Icy Point and Lituya Bay (40–70 km) could potentially generate M_w 7–7.5 earthquakes (Wesnousky, 2008; Stirling et al., 2013); larger events are suggested by the 3.4 m average vertical separation of shorelines on Terrace B (Moss et al., 2022). Complex events that include simultaneous rupture of the Icy Point-Lituya Bay fault (e.g., M_w 7–7.5) and the Fairweather fault (e.g., M_w 7.8) are implied by our results, and could potentially generate M_w 7.9 earthquakes (derived by summing the moments of multiple events (Kanamori, 1983)).

6 Conclusions

The tectonic mechanism driving high rates (>5 km/my) of rock uplift along Earth’s fastest slipping ocean-continent transform plate boundary is a one-sided, positive flower structure along a prominent restraining double bend in the Fairweather fault. Uplifted shorelines at Icy Point record repeated earthquakes coincident with west-side-up displacement on the Fairweather fault and contraction on interconnected reverse faults offshore to the west—a mode of deformation that did not occur during the 1958 M_w 7.8 Fairweather earthquake.

In a region of rapid, present-day uplift caused by post-LIA glacial rebound, tectonic contributions to land-level change can be obscured by isostatic processes. We circumvent this problem by comparing the contrasting RSL histories on either side of the Fairweather fault. Marine terrace elevations and luminescence ages of terrace deposits support estimates of -42.3 ± 2.1 m of RSL change (fall) at Icy Point, west of the Fairweather fault, since sometime between 5.5 and 9.4 ka. East of the fault in Icy Strait, Mann and Streveler (2008) estimated $+4.1 \pm 1/-0.75$ m of RSL change (rise) over the past 6.9–7.2 ka. The difference between the two opposing RSL histories juxtaposed by the fault, amounts to -46.4 ± 2.4 m of RSL change over the past ca. 7 ka driven by tectonic uplift occurring west of the Fairweather fault.

Active fault traces between Lituya Bay and Icy Point delineate a 30-km-long, $\sim 20^\circ$ restraining double bend at the southern end of the Fairweather fault expressed by contractional deformation in the landscape (Witter et al., 2021). Offshore, the Icy Point-Lituya Bay thrust fault (Plafker, 1971; Carlson et al., 1988), imaged in seismic reflection profiles (Balster-Gee et al., 2022a; 2022b), is an east-side-up, buried reverse fault (Figure 2). This offshore reverse fault, and other faults mapped onshore that displace Holocene marine terraces, like the Finger Glacier fault (Witter et al., 2021), reveal a complex fault system that accommodates oblique contractional deformation within the Fairweather fault restraining double bend. We interpret this fault system as an asymmetric, positive flower structure (Figure 13; Woodcock and Fischer, 1986) that decouples deformation of weaker Yakutat sedimentary rocks from stronger oceanic plateau rocks in the lower crust (Lease et al., 2021). Rock uplift rates of 4.6 to 9.0 mm/yr are implied by the uplifted Holocene terraces at Icy Point, and these estimates agree with Quaternary rock exhumation rates of 5–10 km/m.y. (Lease et al., 2021) and late Pleistocene terrace uplift rates of 6–8 m/k.y. (Mann, 1986) occurring within the restraining bend.

Our structural model explains uplift rates observed at Icy Point by invoking variable modes of slip on the Fairweather fault—including strike-slip, vertical-, or oblique-slip during separate earthquakes within the restraining double bend. We suggest that in addition to ruptures like the 1958 Fairweather earthquake, which involved only strike-slip displacement at Icy Point, other earthquakes result from joint rupture of the Fairweather and Icy Point-Lituya Bay faults that collectively uplift coastal terraces and shorten the eastern edge of the Yakutat block that impinges on the North America plate. If the Holocene shorelines on Terrace B at Icy Point record coseismic uplift during past ruptures of the Icy Point-Lituya Bay thrust fault, then our results suggest such earthquakes are relatively rare and occur no more than every 460–1040 years, or roughly one for every 5–10 strike-slip ruptures on the Fairweather fault. Fault rupture scenarios that accommodate convergence require a maximum of 3.1–10 m dip-slip-per-event on an offshore thrust fault and at most a 3–5 m vertical component of slip along the Fairweather fault. Ruptures of the offshore Icy Point-Lituya Bay thrust fault may extend 40–70 km in length along strike and produce M_w 7–7.5 earthquakes accompanied by coseismic uplift of Icy Point. Complex earthquakes that involve simultaneous rupture of both the Icy Point-Lituya Bay thrust fault offshore and the Fairweather fault may reach M_w 7.9.

Acknowledgements

We collaborated with the Army Corps of Engineers' Cold Regions Research and Engineering Lab (CRREL) and the National Center for Airborne Laser Mapping (NCALM) in their development of CRREL's "Helipod" lidar system, which made lidar data acquisition possible in the remote, high-relief, and densely vegetated terrain of western Glacier Bay National Park. Shad O'Neel and Dave Finnegan supported this collaboration; Darren Hauser and Ken Hudnut assisted with data processing. We thank Jim Kearns for boat transport in the field. The U.S. Geological Survey (USGS) Alaska Earthquake Hazards Project and Glaciers and Climate Project funded this research. Thanks to Ben Gaglioti for bringing to our attention the buried stumps near the mouth of Kaknau Creek. Lewis Sharman coordinated permitting for Glacier Bay National Park. Reviews by R. Briggs, D. Mann, A. Meigs, and J. Spotila improved the paper. Any use of trade, firm, or product names is for descriptive purposes only and does not imply endorsement by the U.S. Government.

Availability Statement

All data used in this study may be accessed in U.S. Geological Survey data releases (Balster-Gee et al., 2022a, 2022b; Dartnell et al., 2022; Witter et al., 2017; Witter and Bender, 2022).

References

- Aagaard, B. T., Anderson, G. and Hudnut, K. W. (2004). Dynamic Rupture Modeling of the Transition from Thrust to Strike-Slip Motion in the 2002 Denali Fault Earthquake, Alaska. *B Seismol Soc Am* **94** , S190–S201.
- Aitken, M.J. (1998). An introduction to optical dating, Oxford University Press, 267 pp.
- Anderson, G. and Ji, C. (2003). Static stress transfer during the 2002 Nenana Mountain-Denali Fault, Alaska, earthquake sequence. *Geophys Res Lett* **30** .
- Anderson, R. S. (1990). Evolution of the northern Santa Cruz Mountains by advection of crust past a San Andreas fault bend, *Science*, v. 249, p. 397-401
- Anderson, R. S. (1994). Evolution of the Santa Cruz Mountains, California, through tectonic growth and geomorphic decay, *Journal of Geophysical Research*, v. 999, no. B10, p. 20,161-20,179, doi: 10.1029/94JB00713
- Aston, B.C. (1912). The raised beaches of Cape Turakirae, *Transactions and Proceedings of the New Zealand Institute*, 44, 208-213.
- Auclair, M., Lamothe, M., Huot, S. (2003). Measurement of anomalous fading for feldspar IRSL using SAR. *Radiation Measurements* **37**, 487-492.
- Ave Lallemand, H.G., Kelly, J.S. & Phelps, J.C. (1987). Kinematic analysis of range-front thrust faulting near Anaktuvuk Pass, north-central Brooks Range, Alaska. In: *Alaskan North Slope Geology*. Pacific Section Soc. Econ. Paleont. Mineral, and Alaska Geol. Soc., 639-645.
- Balster-Gee, A.F., Brothers, D.S., Haeussler, P.J., Dartnell, P., Hart, P.E., Wyland, R., and Hatcher, G.A. (2022a). Multichannel minisparker seismic-reflection data collected offshore Glacier Bay National Park during USGS field activity 2015-629-FA: U.S. Geological Survey data Release, <https://doi.org/10.5066/P97Q990F>
- Balster-Gee, A.F., Brothers, D.S., Kluesner, J.W., Miller, N.C., Haeussler, P.J., O'Brien, T.F., Marcuson, R.C., Hart, P.E., Conrad, J.E., Walton, M.L., and Nichols, A.R. (2022b). Multichannel sparker and chirp seismic reflection data collected offshore southeast Alaska during USGS field activity 2017-621-FA: U.S. Geological Survey data release, <https://doi.org/10.5066/P9QXL00L>
- Barnhart, W.D., Briggs, R.W., Reitman, N.G., Gold, R.D., and Hayes, G.P. (2015). Evidence for slip partitioning and bimodal slip behavior on a single fault: Surface slip characteristics of the 2013 M_w 7.7 Balochistan, Pakistan earthquake: *Earth and Planetary Science Letters*, v. 420, p. 1–11, doi: 10.1016/j.epsl.2015.03.027

- Benowitz, J.A., Michele, L., Cooke, M.L., Terhune, P.J., Herreid, S., Bemis, S.P., Toeneboehn, K., Waldien, T.S., and O'Sullivan, P.B., (2021). Why is Denali (6,194 m) so big?: Caught inside the tectonic wake of a migrating restraining bend: *Terra Nova*, [https:// doi .org /10 .1111 /ter .12571](https://doi.org/10.1111/ter.12571)
- Benowitz, J.A., Roeske, S.M., Regan, S.P., Waldien, T.S., Elliott, J.L., and O'Sullivan, P.B., (2022). Large-scale, crustal-block vertical extrusion between the Hines Creek and Denali faults coeval with slip localization on the Denali fault since ca. 45 Ma, Hayes Range, Alaska, USA: *Geosphere*, v. 18, no. 3, p. 1030–1054, <https://doi.org/10.1130/GES02466.1>
- Berryman, K., Clark, K., Cochran, U., Beu, A., and Irwin, S. (2018). A geomorphic and tectonic model for the formation of the flight of Holocene marine terraces at Mahia Peninsula, New Zealand: *Geomorphology*, v. 307, p. 77–92, doi: 10.1016/j.geomorph.2017.10.014
- Brauer, A., Haug, G. H., Dulski, P., Sigman, D. M. & Negendank, J. F. W. (2008). An abrupt wind shift in Western Europe at the onset of the Younger Dryas cold period. *Nature Geosci.* 1, 520–523, <https://doi.org/10.1038/ngeo263>
- Bronk Ramsey, C. (2009). Bayesian analysis of radiocarbon dates: *Radiocarbon*, v. 51, p. 337–360, <https://doi.org/10.1017/S0033822200033865>
- Bronk Ramsey, C. (2023). OxCal 4.4 User Interface: OxCal web page, accessed July 5, 2023, at <https://c14.arch.ox.ac.uk/oxcal/OxCal.html>
- Brothers, D. S., Miller, N.C., Barrie, J.V., Haeussler, P.J., Greene, H.G., Andrews, B.D., Zielke, O., Watt, J., and Dartnell, P. (2020). Plate boundary localization, slip-rates and rupture segmentation of the Queen Charlotte Fault based on submarine tectonic geomorphology, *Earth and Planetary Science Letters* 530, p. 115882, doi: 10.1016/j.epsl.2019.115882
- Bruhn, R.L., Pavlis T.L., Plafker G., Serpa L. (2004). Deformation during terrane accretion in the Saint Elias orogen, Alaska, *Geological Society of America Bulletin*, v. 116. p. 771–787.
- Bruhn, R.L., Sauber, J., Cotton, M.M., Pavlis, T.L., Burgess, E., Ruppert, N., and Forster, R.R. (2012). Plate margin deformation and active tectonics along the northern edge of the Yakutat terrane in the Saint Elias orogen, Alaska, and Yukon, Canada: *Geosphere*, v. 8, p. 1384–1407, [https:// doi .org /10 .1130 /GES00807 .1](https://doi.org/10.1130/GES00807.1)
- Bruns, T.R. (1983). Model for the origin of the Yakutat block, an accreted terrane in the northern Gulf of Alaska: *Geology*, v. 11, no. 12, p. 718–721, [https:// doi .org /10 .1130 /0091 -7613\(1983\)11 <718: MFTOOT>2 .0 .CO;2](https://doi.org/10.1130/0091-7613(1983)11<718:MFTOOT>2.0.CO;2)
- Burgmann, R., Arrowsmith, J. R., Dumitru, T., and McLaughlin, R. (1994). Rise and fall of the southern Santa Cruz Mountains, California, from fission tracks, geomorphology, and geodesy, *Journal of geophysical Research*, v.99, no. B10 p. 20,181-20,202, doi:10.1029/94JB00131
- Carlson, P.R., Plafker, G. and Bruns, T.R. (1985). Map and selected seismic profiles of the seaward extension of the Fairweather fault, eastern Gulf of Alaska, U. S. Geological Survey Miscellaneous Field Studies Map MF 1722, 2 sheets.
- Carlson, P.R., Bruns, T.R. and Plafker, G. (1988). Late Cenozoic offsets on the offshore connection between the Fairweather and Queen Charlotte faults off southeast Alaska. *Mar. Geol.*, 85: 89-97.
- Casas, A. M., Gapais, D., Nalpas, T., Besnard, K. and Roman-Berdiel, T. (2001). Analogue models of transpressive systems. *J. Struct. Geol.* 23, 733–743.
- Christeson, G.L., Gulick, S.P.S., van Avendonk, H.J.A., Worthington, L.L., Reece, R.S., and Pavlis, T.L. (2010). The Yakutat terrane: Dramatic change in crustal thickness across the Transition fault, Alaska: *Geology*, v. 38, p. 895–898, doi: 10.1130/G31170.1

- Cowgill, E., Yin, A., Arrowsmith, J. R., Feng, W. X. and Shuanhong, Z. (2004). The Akato Tagh bend along the Altyn Tagh fault, northwest Tibet 1: Smoothing by vertical-axis rotation and the effects of topographic stresses on bend-flanking faults, *Geological Society of America Bulletin*, v. 116, p. 1423-1442.
- Crowell, J. C. (1974). Origin of late Cenozoic basins in southern California, in Dickinson, W. R., ed., *Tectonics and Sedimentation*, Society of Economic Paleontologists and Mineralogists: Tulsa, Oklahoma, Special Publication 22, p. 190-204.
- Crowell, A.L., Howell, W.K., Mann, D.H., and Streveler, G.P. (2013). The Hoonah Tlingit Cultural Landscape in Glacier Bay National Park and Preserve: An Archaeological and Geological Study, U.S. Department of the Interior, National Park Service, Gustavus, AK: <http://npshistory.com/publications/glba/hoonah-tlingit.pdf>
- Cunningham, W. D. and Mann, P. (2007). Tectonics of strike-slip restraining and releasing bends: *Geological Society, London, Special Publications* 290, 1–12.
- Dartnell, P., Brothers, D.S., and Haeussler, P.J. (2022). Multibeam bathymetry and acoustic-backscatter data collected in 2015 near Cross Sound, southeast Alaska, during field activity 2015-629-FA: U.S. Geological Survey data release, <https://doi.org/10.5066/F7JH3KG6>
- Doser, D.I. (2010). A Reevaluation of the 1958 Fairweather, Alaska, Earthquake Sequence: *Bulletin of the Seismological Society of America*, v. 100, p. 1792–1799, doi: 10.1785/0120090343
- Doser, D.I., and Lomas, R. (2000). The transition from strike-slip to oblique subduction in southeastern Alaska from seismological studies, *Tectonophysics*, v. 316, p. 45–65, doi: 10.1016/S0040-1951(99)00254-1
- Eberhart-Phillips, D., Haeussler, P. and Freymueller, J. (2003). The 2002 Denali fault earthquake, Alaska: a large magnitude, slip-partitioned event. *Science* .
- Eberhart-Phillips, D. et al. (2006). Imaging the transition from Aleutian subduction to Yakutat collision in central Alaska, with local earthquakes and active source data. *Journal of Geophysical Research*, 111.
- Elliott, J.L., Larsen, C.F., Freymueller, J.T., and Motyka, R.J. (2010). Tectonic block motion and glacial isostatic adjustment in southeast Alaska and adjacent Canada constrained by GPS measurements. *Journal of Geophysical Research*, v. 115, doi:10.1029/2009JB007139
- Elliott, J., and Freymueller, J.T. (2020). A Block Model of Present-Day Kinematics of Alaska and Western Canada: *Journal of Geophysical Research: Solid Earth*, v. n/a, p. e53951, doi:10.1029/2019JB018378
- Fitzgerald, P. G. Roeske, S.M., Benowitz, J.A., Riccio, S.J., Perry, S.E., and Armstrong, P.A. (2014). Alternating asymmetric topography of the Alaska range along the strike-slip Denali fault: Strain partitioning and lithospheric control across a terrane suture zone: *Tectonics*, 33, doi:10.1002/(issn)1944-9194.
- Fleming, K., Johnston, P., Zwartz, D., Yokoyama, Y., Lambeck, K., & Chappell, J. (1998). Refining the eustatic sea-level curve since the Last Glacial Maximum using far- and intermediate-field sites. *Earth and Planetary Science Letters* , 163 (1–4), 327–342. [https://doi.org/10.1016/s0012-821x\(98\)00198-8](https://doi.org/10.1016/s0012-821x(98)00198-8)
- Galbraith, R.F., and Roberts, R.G. (2012). Statistical aspects of equivalent dose and error calculation and display in OSL dating: An Overview and some recommendations. *Quaternary Geochronology* 11, 1-27.
- Gray, H.J., Mahan, S.A., Rittenour, T., and Nelson, M. (2015). Guide to luminescence dating techniques and their application for paleoseismic research, in: W. R. Lund (ed.), *Basin and range province seismic hazards summit III*, Salt Lake City, UT, Utah Geological Survey Miscellaneous Publication.
- Hayes, G., Briggs, R. W., Sladen, A., Fielding, E. J., Prenticxe, C., Hudnut, K., Mann, P., Taylor, F. W., Crone, A. J., Gold, R., and Simons, M. (2010). Complex rupture during the 12 January 2010 Haiti earthquake, *Nature Geoscience* 3, 800–805.

- Heaton, T.J., Kohler, P., Butzin, M., Bard, E., Reimer, R.W., Austin, W.E.N., Bronk Ramsey, C., Grootes, P.M., Hughen, K.A., Kromer, B., Reimer, P.J., Adkins, J., Burke, A., Cook, M.S., et al. (2020). Marine20 - The Marine Radiocarbon Age Calibration Curve (0-55,000 cal BP): Radiocarbon, v. 62, p. 779–820, doi: 10.1017/RDC.2020.68
- Hudson, T., Plafker, G., and Rubin, M. (2022). Tectonic controls on marine terrace origin and character in the Lituya Bay area, eastern Gulf of Alaska: Alaska Division of Geological & Geophysical Surveys Report of Investigation 2022-4, 27 p. <https://doi.org/10.14509/30903>
- Huntley, D.J. and Lamothe, M. (2001). Ubiquity of anomalous fading in K-feldspars and the measurement and correction for it in optical dating. *Can. J. Earth Sci.* 38, 1093–1106.
- Kanamori, H. (1983). Magnitude scale and quantification of earthquakes, *Tectonophysics*, 93: 185–199.
- Kelsey, H.M., (2015). Geomorphological indicators of past sea levels, in: Shennan, I., Long, A.J., Horton, B.P., eds., *Handbook of Sea-Level Research*, Chapter 5, p.66-82, John Wiley & Sons, Chichester. ISBN: 978-1-118-45258-5.
- Lahr, J. C , and G. Plafker (1980). Holocene Pacific-North American plate interaction in southern Alaska: Implications for the Yakataga seismic gap: *Geology*, v. 8, p. 483-486.
- Lajoie, K.R. (1986). Coastal tectonics, *in* *Active Tectonics*, p. 95-124, National Academy Press, Washington, D.C., ISBN 0-309-03638-0
- Lease, R.O., Haeussler, P. J., Witter, R. C., Stockli, D. F., Bender, A. M., Kelsey, H. M. and O’Sullivan, P. B. (2021). Extreme Quaternary plate boundary exhumation and strike slip localized along the southern Fairweather fault, Alaska, USA: *Geology*, v. 49, p. 602-606, <https://doi.org/10.1130/G48464.1>
- Lin, J. and Stein, R. S. (2004). Stress triggering in thrust and subduction earthquakes and stress interaction between the southern San Andreas and nearby thrust and strike-slip faults. *J Geophys Res Solid Earth* **109**.
- Little, T.A., Van Dissen, R., Schermer, E. and Carne, R. (2009). Late Holocene surface ruptures on the southern Wairarapa fault, New Zealand: Link between earthquakes and the uplifting of beach ridges on a rocky coast, *Lithosphere*, 1, 4-28.
- Loney, R.A., and Himmelberg, G.R. (1983). Structure and petrology of the La Perouse gabbro intrusion, Fairweather Range, southeastern Alaska: *Journal of Petrology*, v. 24, p. 377–423, <https://doi.org/10.1093/petrology/24.4.377>
- Mann, D.H. (1986). Wisconsin and Holocene glaciation of southeast Alaska. In T.D. Hamilton et al. (Editors), *Glaciation in Alaska – The Geologic Record*, Proc. Alaska Geol. Soc. 237-265.
- Mann, P. (2007). Global catalogue, classification and tectonic origins of restraining- and releasing bends on active and ancient strike-slip fault systems. Geological Society, London, Special Publications 290, 13–142.
- Mann, D.H. and Ugolini, F.C. (1985). Holocene glacial history of the Lituya District, southeast Alaska. *Canadian Journal of Earth Sciences*, 22(6), pp.913-928.
- Mann, D. H., and Streveler, G. P. (2008). Post-glacial relative sea level, isostasy, and glacial history in Icy Strait, Southeast Alaska, USA. *Quaternary Research*, 69(2), 201–216. <https://doi.org/10.1016/j.yqres.2007.12.005>
- Marincovich, L. (1980). Miocene mollusks of the Topsy Formation, Lituya District, Gulf of Alaska Tertiary Province, Alaska: U.S. Geological Survey Professional Paper 1125C, 14 p.
- McAlear, R.J., Spotila, J.A., Enkelmann, E., and Berger, A.L. (2009). Exhumation along the Fairweather fault, southeastern Alaska, based on low-temperature thermochronometry: *Tectonics*, v. 28, p. n/a–n/a, doi: 10.1029/2007TC002240

- McSaveney, M.J., Graham, I.J., Begg, J.G., Beau, A.G., Hull, A.G., Kim, K., and Zondervan, A. (2006). Late Holocene uplift of beach ridges at Turakirae Head, south Wellington coast, New Zealand, *New Zealand Journal of Geology and Geophysics*, 49, 337-358.
- Miller, D.J. (1960). Giant waves in Lituya Bay, Alaska. United States Geological Survey, Professional Paper 354-C, p. 51-86.
- Miller, D.J. (1961). Geology of the Lituya District, Gulf of Alaska Tertiary Province, Alaska, U. S. Geological Survey Open-File Report OFR 61-100 scale 1:96,000.
- Molnar, P. and Dayem, K.E. (2010). Major intracontinental strike-slip faults and contrasts in lithospheric strength, *Geosphere*, v. 6, p. 444–467, doi: 10.1130/GES00519.1
- Moss, R., Thompson, S., Kuo, C., Younesi, K., Chao, S. (2022). Report GIRS 2022-05: Reverse Fault PFDHA, University of California (Los Angeles), DOI: 10.34948/N3F595.
- Namson, J. and T. L. Davis (1990). Late Cenozoic Fold and Thrust Belt of the Southern Coast Ranges and Santa Maria Basin, California (1). *AAPG Bulletin*, 74. <https://doi.org/10.1306/0c9b2335-1710-11d7-8645000102c1865d>
- Nelson, A.R. and Manley, W.F. (1992). Holocene coseismic and aseismic uplift of Isla Mocha, south-central Chile, *Quaternary International*, 15/16, 61-76.
- Okuwaki, R., and Fan, W. (2022). Oblique convergence causes both thrust and strike-slip ruptures during the 2021 M 7.2 Haiti earthquake. *Geophysical Research Letters*, 49, e2021GL096373. <https://doi.org/10.1029/2021GL096373>
- Ota, Y., Hull, A.G., and Berryman, K.R. (1991). Coseismic Uplift of Holocene Marine Terraces in the Pakarae River Area, Eastern North Island, New Zealand: *Quaternary Research*, v. 35, p. 331–346, doi: 10.1016/0033-5894(91)90049-B
- Pavlis, T. L., Picornell, C., Serpa, L., Bruhn, R. L., & Plafker, G. (2004). Tectonic processes during oblique collision: Insights from the St. Elias orogen, northern North American Cordillera. *Tectonics*, 23(3). <https://doi.org/10.1029/2003tc001557>
- Plafker, G. (1967). Geologic map of the Gulf of Alaska Tertiary province, Alaska: U.S. Geol. Survey Misc. Geol. Inv. Map 1-484, scale 1:500,000. (1 in. equals about 8 miles.)
- Plafker, G. (1971). Petroleum and Coal, p. 85-88, *in* MacKevett, E. M., Brew, D. A., Hawley, C. C., Huff, L. C. and Smith, J. G., 1971, Mineral Resources of Glacier Bay National Monument, Alaska, U. S. Geological Survey Professional Paper 632, 90 pp and 12 plates, <https://doi.org/10.3133/pp632>
- Plafker, G., Hudson, T., Bruns, T.R. and Rubin, M. (1978). Late Quaternary offsets along the Fairweather Fault and crustal plate interactions in southern Alaska, *Canadian Journal of Earth Science*, v. 15 p. 805-816.
- Plafker, G. (1987). Regional geology and petroleum potential of the northern Gulf of Alaska continental margin, Circum-Pacific Council for Energy and Mineral Resources, *Geology and Resource Potential of the Western North America and Adjacent Ocean Basins—Beaufort Sea to Baja California*, v. 6, Chapter 11, p. 229-268.
- Plafker, G., Gilpin, L. M., & Lahr, J. C. (1994). Neotectonic map of Alaska. In G. Plafker, & H. C. Berg (Eds.). *The Geology of Alaska: The Geology of North America*. v. G1, Plate 12, 1 sheet with text, scale 1:2,500,000. Boulder, CO: Geological Society of America.
- Plafker, G., and W. Thatcher (2008). Geological and geophysical evaluation of the mechanism of the great 1899 Yakutat Bay Earthquake, in *Active Tectonics and Seismic Potential of Alaska*, edited by J. T. Freymueller et al., pp. 215–236, AGU, Washington, D. C.

- Pratt, T.L., Troost, K.G., Odum, J.K. and W.J. Stephenson, (2015). Kinematics of shallow backthrusts in the Seattle fault zone, Washington State. *Geosphere*, 11 (6), pp.1948-1974.
- Rasmussen, S. O. et al. (2006). A new Greenland ice core chronology for the last glacial termination. *J. Geophys. Res.* 111, D06102
- Reimer, P.J., Austin, W.E.N., Bard, E., Bayliss, A., Blackwell, P.G., Bronk Ramsey, C., Butzin, M., Cheng, H., Edwards, R.L., Friedrich, M., Grootes, P.M., Guilderson, T.P., Hajdas, I., Heaton, T.J., et al. (2020). The IntCal20 Northern Hemisphere Radiocarbon Age Calibration Curve (0–55 cal kBP): Radiocarbon, v. 62, p. 725–757, doi: 10.1017/RDC.2020.41
- Reimer, P.J., and Reimer, R.W. (2001). A marine reservoir correction database and on-line interface. *Radiocarbon* 43(2A):461–463. doi: 10.1017/S0033822200038339
- Rollins, C., Freymueller, J.T., Sauber, J.M. (2020). Stress Promotion of the 1958 M_w 7.8 Fairweather Fault Earthquake and Others in Southeast Alaska by Glacial Isostatic Adjustment and Inter-earthquake Stress Transfer, *Journal of Geophysical Research*, v. 126, n. 1, <https://doi.org/10.1029/2020JB020411>
- Rubin, M., and Alexander, C. (1958). U.S. Survey radiocarbon dates IV; *Science*, v. 127, no. 3313, p. 1476-1487.
- Schartman, A., Enkelmann, E., Garver, J. I., & Davidson, C. M. (2019). Uplift and exhumation of the Russell Fiord and Boundary blocks along the northern Fairweather transform fault, Alaska. *Lithosphere*, 1–20. <https://doi.org/10.1130/11011.1>
- Shennan, I. (2015). Handbook of sea-level research: framing research questions. In: Shennan, I., Long, A.J., Horton, B.P. (Eds.), *Handbook of Sea-Level Research*. Wiley, Chichester, pp. 3–25. <https://doi.org/10.1002/9781118452547.ch2>
- Shennan, I., Milne, G., and Bradley, S. (2012). Late Holocene vertical land motion and relative sea-level changes: lessons from the British Isles. *Journal of Quaternary Science*, 27, 64–70.
- Siddall, M., E. J. Rohling, W. G. Thompson, and C. Waelbroeck (2008). Marine isotope stage 3 sea level fluctuations: Datasynthesis and new outlook, *Rev. Geophys.*, 46, RG4003, doi:10.1029/2007RG000226
- Simms, A. R., Rouby, H. & Lambeck, K. (2015). Marine terraces and rates of vertical tectonic motion: The importance of glacio-isostatic adjustment along the Pacific coast of central North America. *Geological Society of America Bulletin* 128, <https://doi.org/10.1130/B31299.1>
- Spotila, J. A., Farley, K. A., Yule, J. D., and Reiners, P. W. (2001). Near-field transpressive deformation along the San Andreas fault zone in southern California, based on exhumation constrained by (U-Th)/He dating, *Journal of Geophysical Research*, v. 106, no. B12, p. 30,909-30,922, doi: 10.1029/2001JB000348
- Spotila, J.A., Niemi, N., Brady, R., House, M., Buscher, J., and Oskin, M. (2007). Long-term continental deformation associated with transpressive plate motion: The San Andreas fault: *Geology*, v. 35, p. 967–4, doi: 10.1130/G23816A.1
- Stirling, M., Goded, T., Berryman, K., & Litchfield, N. (2013). Selection of Earthquake Scaling Relationships for Seismic-Hazard Analysis, *Bulletin of the Seismological Society of America*, 103(6), 2993–3011. <https://doi.org/10.1785/0120130052>
- Sylvester, A. G. & Smith, R. R. (1976). Tectonic transpression and basement-controlled deformation in San Andreas fault zone, Salton Trough, California. *Bull. Am. Ass. Petrol. Geol.* 57, 74-96.
- ten Brink, U. S., Miller, N. C., Andrews, B. D., Brothers, D. S., & Haeussler, P. J. (2018). Deformation of the Pacific/North America Plate Boundary at Queen Charlotte Fault: The Possible Role of Rheology. *Journal of Geophysical Research: Solid Earth*, 123. <https://doi.org/10.1002/2017jb014770>

- Tocher, D. (1960). The Alaska earthquake of July 10, 1958: Movement on the Fairweather fault and field investigation of southern epicentral region. *Bulletin of the Seismological Society of America*, v. 50, p. 267–292.
- Tocher, D., & Miller, D.J. (1959). Field observations on effects of Alaska earthquake of 10 July 1958. *Science*, v. 129, p. 394–395.
- Toeneboehn, K., Cooke, M. L., Bemis, S. P., Fendick, A. M. and Benowitz, J. (2018). Stereovision Combined With Particle Tracking Velocimetry Reveals Advection and Uplift Within a Restraining Bend Simulating the Denali Fault. *Frontiers Earth Sci.* 6, 152, doi: 10.3389/feart.2018.00152.
- Trenhaile, A.S. (1972). The shore platforms of the Vale of Glamorgan, Wales. *Transactions of the Institute of British Geographers*, 56, 127–144.
- Ugolini, F.C. and Mann, D.H. (1979). Biopedological origin of peatlands in southeast Alaska, *Nature*, 281, 366–368.
- U.S. Geological Survey (2016). 5-meter Alaska Digital Elevation Models (DEMs)—USGS National Map 3DEP Downloadable Data Collection, accessed April 3, 2017 at <http://nationalmap.gov/3DEP/>.
- Wallinga, J., Murray, A., Wintle, A. (2000). The single-aliquot regenerative-dose (SAR) protocol applied to coarse-grain feldspar. *Radiation Measurements* 32, 529–533.
- Walton, M. A., Gulick, S. P., & Haeussler, P. J. (2022). Revisiting the 1899 earthquake series using integrative geophysical analysis in Yakutat Bay, Alaska, USA. *Geosphere*, 18(5), 1453–1473. <https://doi.org/10.1130/GES02423.1>
- Wellman, H.W. (1969). Tilted marine beach ridges at Cape Turakirae, New Zealand, *Tuatara*, 17, 82–93
- Wesnousky, S. G. (2005). The San Andreas and Walker Lane fault systems, western North America: transpression, transtension, cumulative slip and the structural evolution of a major transform plate boundary. *J Struct Geol* 27, 1505–1512.
- Wesnousky, S. G. (2008). Displacement and Geometrical Characteristics of Earthquake Surface Ruptures: Issues and Implications for Seismic-Hazard Analysis and the Process of Earthquake Rupture. *Bulletin of the Seismological Society of America*, 98(4), 1609–1632. <https://doi.org/10.1785/0120070111>
- Wilson, F.H., Hulst, C.P., Mull, C.G., and Karl, S.M. (2015). Geologic map of Alaska: U.S. Geological Survey Scientific Investigations Map 3340, 2 sheets, scale 1:1,584,000, with 196 p. text, <https://doi.org/10.3133/sim3340>
- Witter, R.C., LeWinter, A., Bender, A.M., Glennie, C., and Finnegan, D. (2017a). Sculpted by water, elevated by earthquakes—The coastal landscape of Glacier Bay National Park, Alaska: U.S. Geological Survey General Information Product 177, doi:10.3133/gip177
- Witter, R.C., and Bender, A.M. (2021). Radiocarbon and luminescence data for Fairweather fault investigation, Glacier Bay National Park, southeast Alaska (ver 2.0, July 2023): U.S. Geological Survey data release, <https://doi.org/10.5066/P9Q08JGV>
- Witter, R.C., LeWinter, A., Glennie, C., Hauser, D., Bender, A., Finnegan, D. (2017b). Digital Elevation Models of Glacier Bay National Park, Between Lituya Bay and Icy Point, Alaska, Derived from Airborne Lidar Data Acquired in September 2015: U.S. Geological Survey data release, <https://doi.org/10.5066/F7W094D4>
- Witter, R. C., Bender, A. M., Scharer, K. M., DuRoss, C. B., Haeussler, P. J., & Lease, R. O. (2021). Geomorphic expression and slip rate of the Fairweather fault, southeast Alaska, and evidence for predecessors of the 1958 rupture. *Geosphere*, 17(3), 711–738. <https://doi.org/10.1130/ges02299.1>

Woodcock, N.H., and Fischer, M. (1986). Strike-slip duplexes: *Journal of Structural Geology*, v. 8, p. 725–735, doi: 10.1016/0191-8141(86)90021-0

Table 1. Infrared Stimulated Luminescence (IRSL) age information (Witter and Bender, 2021)

Sample no. (Lab no.)*	IRSL age $\pm 2\sigma$ (ka) [§]	DE $\pm 2s$ (Gy) [Age model] ⁺	Lat, Long (degrees) [#]	Elevation(m), date	Elevation(m), date	Geologic setting	
17IP-10-8A (USU-2694)	4.18 \pm 1.39	2.33 \pm 0.74 [MAM]	58.397160, -137.089075	57 m, 5/31/17	Dune crest on highest part of Terrace B, sample depth = 105 cm. Uncon- solidated laminated medium-to- fine-grained sand.	Dune crest on highest part of Terrace B, sample depth = 105 cm. Uncon- solidated laminated medium-to- fine-grained sand.	Dune crest on highest part of Terrace B, sample depth = 105 cm. Uncon- solidated laminated medium-to- fine-grained sand.
17IP-10-7A, (USU-2693)	4.74 \pm 1.10	3.22 \pm 0.68 [CAM]	58.397160, -137.089075	57 m, 5/31/17	Dune crest overlying the highest part of Terrace B, sample depth = 142 cm. Uncon- solidated laminated medium-to- fine-grained sand.	Dune crest overlying the highest part of Terrace B, sample depth = 142 cm. Uncon- solidated laminated medium-to- fine-grained sand.	Dune crest overlying the highest part of Terrace B, sample depth = 142 cm. Uncon- solidated laminated medium-to- fine-grained sand.
17IP-28-2A, (USU-2696)	4.39 \pm 0.66	4.16 \pm 0.51 [CAM]	58.400163, -137.080493	35 m, 6/6/17	Tocher's Gulch, sample depth = 270 cm below shoreline B8 of Terrace B, beach sand with heavy mineral laminations.	Tocher's Gulch, sample depth = 270 cm below shoreline B8 of Terrace B, beach sand with heavy mineral laminations.	Tocher's Gulch, sample depth = 270 cm below shoreline B8 of Terrace B, beach sand with heavy mineral laminations.

Sample no. (Lab no.)*	IRSL age $\pm 2\sigma$ (ka) [§]	DE $\pm 2s$ (Gy) [Age model]+	Lat, Long (degrees) [#]	Elevation(m), date	Elevation(m), date	Geologic setting	
17IP-28-1A, (USU-2695)	5.99 ± 1.02	4.01 ± 0.58 [MAM]	58.400163, -137.080493	35 m, 6/6/17	Tocher's Gulch, sample depth = 389 cm below shoreline B8 of Terrace B, beach sand with heavy mineral laminations, cobble (few).	Tocher's Gulch, sample depth = 389 cm below shoreline B8 of Terrace B, beach sand with heavy mineral laminations, cobble (few).	Tocher's Gulch, sample depth = 389 cm below shoreline B8 of Terrace B, beach sand with heavy mineral laminations, cobble (few).
17IP-30-1A, (USU-2697)	5.98 ± 1.71	4.28 ± 1.16 [MAM]	58.406014, -137.084810	20 m, 5/30/17; 6/6/17	Trident Channel (Fig. 5), sample depth = 134 cm, laminated- to-cross- laminated flu- vial/beach sand and gravel.	Trident Channel (Fig. 5), sample depth = 134 cm, laminated- to-cross- laminated flu- vial/beach sand and gravel.	Trident Channel (Fig. 5), sample depth = 134 cm, laminated- to-cross- laminated flu- vial/beach sand and gravel.

Sample no. (Lab no.)*	IRSL age $\pm 2\sigma$ (ka) [§]	DE $\pm 2s$ (Gy) [Age model] ⁺	Lat, Long (degrees) [#]	Elevation(m), date	Elevation(m), date	Geologic setting	
*Analyses performed by Utah State University (USU) Luminescence Laboratory. Age analysis using the single-aliquot regenerative-dose procedure of Wallinga et al. (2000) on 2mm small-aliquots of feldspar sand at 50°C IRSL. Number of aliquots used in age calculation and number of aliquots analyzed in parentheses. [§] IRSL age on each aliquot corrected for fading following the method by Auclair et al. (2003) and correction model of Huntley and Lamothe (2001). +Equivalent dose	*Analyses performed by Utah State University (USU) Luminescence Laboratory. Age analysis using the single-aliquot regenerative-dose procedure of Wallinga et al. (2000) on 2mm small-aliquots of feldspar sand at 50°C IRSL. Number of aliquots used in age calculation and number of aliquots analyzed in parentheses. [§] IRSL age on each aliquot corrected for fading following the method by Auclair et al. (2003) and correction model of Huntley and Lamothe (2001). +Equivalent dose	*Analyses performed by Utah State University (USU) Luminescence Laboratory. Age analysis using the single-aliquot regenerative-dose procedure of Wallinga et al. (2000) on 2mm small-aliquots of feldspar sand at 50°C IRSL. Number of aliquots used in age calculation and number of aliquots analyzed in parentheses. [§] IRSL age on each aliquot corrected for fading following the method by Auclair et al. (2003) and correction model of Huntley and Lamothe (2001). +Equivalent dose	*Analyses performed by Utah State University (USU) Luminescence Laboratory. Age analysis using the single-aliquot regenerative-dose procedure of Wallinga et al. (2000) on 2mm small-aliquots of feldspar sand at 50°C IRSL. Number of aliquots used in age calculation and number of aliquots analyzed in parentheses. [§] IRSL age on each aliquot corrected for fading following the method by Auclair et al. (2003) and correction model of Huntley and Lamothe (2001). +Equivalent dose	*Analyses performed by Utah State University (USU) Luminescence Laboratory. Age analysis using the single-aliquot regenerative-dose procedure of Wallinga et al. (2000) on 2mm small-aliquots of feldspar sand at 50°C IRSL. Number of aliquots used in age calculation and number of aliquots analyzed in parentheses. [§] IRSL age on each aliquot corrected for fading following the method by Auclair et al. (2003) and correction model of Huntley and Lamothe (2001). +Equivalent dose	*Analyses performed by Utah State University (USU) Luminescence Laboratory. Age analysis using the single-aliquot regenerative-dose procedure of Wallinga et al. (2000) on 2mm small-aliquots of feldspar sand at 50°C IRSL. Number of aliquots used in age calculation and number of aliquots analyzed in parentheses. [§] IRSL age on each aliquot corrected for fading following the method by Auclair et al. (2003) and correction model of Huntley and Lamothe (2001). +Equivalent dose	*Analyses performed by Utah State University (USU) Luminescence Laboratory. Age analysis using the single-aliquot regenerative-dose procedure of Wallinga et al. (2000) on 2mm small-aliquots of feldspar sand at 50°C IRSL. Number of aliquots used in age calculation and number of aliquots analyzed in parentheses. [§] IRSL age on each aliquot corrected for fading following the method by Auclair et al. (2003) and correction model of Huntley and Lamothe (2001). +Equivalent dose	*Analyses performed by Utah State University (USU) Luminescence Laboratory. Age analysis using the single-aliquot regenerative-dose procedure of Wallinga et al. (2000) on 2mm small-aliquots of feldspar sand at 50°C IRSL. Number of aliquots used in age calculation and number of aliquots analyzed in parentheses. [§] IRSL age on each aliquot corrected for fading following the method by Auclair et al. (2003) and correction model of Huntley and Lamothe (2001). +Equivalent dose

Sample no. (Lab no.)*	IRSL age $\pm 2\sigma$ (ka) [§]	DE $\pm 2s$ (Gy) [Age model] ⁺	Lat, Long (degrees) [#]	Elevation(m), date	Elevation(m), date	Geologic setting
--------------------------	---	---	-------------------------------------	-----------------------	-----------------------	---------------------

Table 2. Icy Point radiocarbon data (Witter and Bender, 2021)

Sample ID	Analytical age* (¹⁴ C yrs BP)	Calibrated age (cal yr BP) [§]	Description of material submitted
17IP-26-1	>Modern	–	Picea needle fragment picked from bulk t
17IP-33-1B-29	145±20	280-0	Sub-sample of ring 29 from buried growth
17IP-33-1B	165±15	290-0	Sub-sample of rings 7–9 from buried growth
17IP-5-S1	1,070±20	400-30 [#]	Marine bivalve shell from pit on Terrace
17IP-33-1B-79A	310±20	450-300	Sub-sample of ring 79 from buried growth
17IP-33-1B-79B	260±20	420-160	Sub-sample of ring 79 from buried growth
17IP-33-1B-79C**	285±15	430-300	Combined result of replicate analyses of
17IP-34-6B	705±20	680-570	Sub-sample of ring 16 from formerly buried
17IP-34-6B-26	755±35	730-660	Sub-sample of ring 26 from formerly buried
17IP-16-4A	1,210±25	1240-1060	Conifer needles from ponded sediment over

Table 2. Icy Point radiocarbon data (continued)

Sample ID

Landform	Elevation (m) change per km
<i>Slopes of Icy Point marine terraces parallel to Fairweather fault</i>	<i>Slopes of Icy Point marine terraces parallel to Fair</i>
Terrace C profile H–H'	2–16
Terrace B profile K–K'	14
<i>Slopes of Icy Point marine terraces perpendicular to Fairweather fault</i>	<i>Slopes of Icy Point marine terraces perpendicular t</i>
Terrace C profile I–I'	40
Terrace C profile J–J'	15–28
<i>Gradients of modern platforms in central California</i>	<i>Gradients of modern platforms in central Californi</i>
Inshore platform	20–40

Landform	Elevation (m) change per km
Offshore platform	7–17

Table 4. Parameters used to estimate tectonic uplift component of Holocene relative sea-level change at Icy Point

Parameter	Height (m)
<i>Parameters used to estimate Holocene RSL change at Icy Point</i>	
(A) Terrace B inner edge*	47.3
(B) Terrace B sediment thickness	3
(C) Terrace B shoreline angle [§]	44.3
(D) Modern shoreline angle ⁺	2.0
(E) RSL change at Icy Point [#]	-42.3
<i>Holocene RSL change in Icy Strait</i>	
(F) RSL change in Icy Strait**	4.1
<i>Difference between Icy Point and Icy Strait Holocene RSL change</i>	
(G) Tectonic component of RSL change at Icy Point	-46.4

*The height of the inner edge is the elevation (m, NAVD 88) at the sharpest inflection in slope along the base of the sea cliff backing Terrace B.

[§]Estimated as the difference between the inner edge height and sediment thickness; $C = A - B$

⁺The height of the the modern shoreline angle is the elevation (m, NAVD 88) at the base of the slope between the modern shore platform and Terrace A.

[#]Icy Point RSL change; $E = D - C$; see text for explanation. Error calculated as the square-root of the sum of squared errors of parameters A–C.

**Holocene RSL change and uncertainty reported by Mann and Streveler (2008).

Table 5. Estimates of fault-normal shortening rates and dip slip-per-event for the Icy Point-Lituya Bay thrust fault assuming simple fault geometries that splay off the Fairweather fault.

Reverse fault dip angle (degrees)	Fault inter-section depth (km) ^a	Holocene uplift rate (mm/yr) ^b	Fault-normal rate (mm/yr) ^c
30	2.9	5–9	8.6–15.6
45	5.0	5–9	5–9
60	8.7	5–9	2.9–5.2
75	18.7	5–9	1.3–2.4

^aDepth calculated by multiplying the tangent of the dip angle by the distance between the reverse fault and the Fairweather fault (~5 km) assuming planar fault geometries.

^bUplift rate estimated by this study.

^cFault-normal (shortening) rate calculated by dividing the uplift rate by the tangent of the dip angle.

^dCoseismic uplift estimated from heights of terrace risers measured at Icy Point.

^eSlip estimates calculated by dividing the range of uplift estimates by the sine of the dip angle.

Appendix

OxCal (version 4.4.2, Bronk Ramsey, 2009; 2023) model code used to compute the master age chronology shown on Figure 8.

```
Plot("ICY POINT MASTER CHRONOLOGY")
{
Sequence("Age of terrace B shoreline angle")
{
Boundary("START: Kaknau Lake time");
Phase("Kaknau Lake deposits")
{
R_Date("17IP-18-7", 9510, 45);
R_Date("17IP-18-10", 9320, 45);
};
Date("Kaknau Lake drains");
Phase("Outwash deposits")
{
R_Date("17IP-13-S5", 8780, 40);
R_Date("17IP-14", 8660, 80);
R_Date("17IP-15-S1", 8650, 40);
R_Date("17IP-15-S3", 8390, 40);
R_Date("17IP-15-S4", 8350, 75);
};
Date("TERRACE B SHORELINE ANGLE");
Phase("Terrace B beach sand")
{
C_Date("17IP-28-1A", -3973, 1020);
C_Date("17IP-28-2A", -2373, 660);
};
Phase("Terrace B dune sand")
{
C_Date("17IP-10-7A", -2723, 1100);
C_Date("17IP-10-8A", -2163, 1390);
};
Phase("Kaknau Creek terrace gravel")
{
R_Date("17IP-17-S1", 1560, 35);
```

```
R_Date("17IP-16-4B", 1300, 25);
R_Date("17IP-20-1C", 1260, 15);
R_Date("17IP-16-4A", 1210, 25);
};
D_Sequence("Stump 34-6B")
{
Boundary("Stump 34 sprouts");
Gap(6);
R_Date("Ring 26", 755, 35);
Gap(9);
R_Date("Ring 16", 705, 20);
Gap(15);
Boundary("Stump 34 death");
};
D_Sequence("Stump 33-1B")
{
Boundary("Stump 33 sprouts");
Gap(16);
R_Date("17IP-33-1B-79C", 285, 15);
Gap(49);
R_Date("Ring 29", 145, 20);
Gap(28);
Boundary("Stump 33 death");
};
C_Date("Onset of rapid glacier rebound", 1775, 12.5);
Boundary("Terrace A time");
};
};
```